Thermal evolution of Pluto and implications for surface tectonics and a sub-surface ocean

Guillaume Robuchon*[a], Francis Nimmo[a]

[a] *Department of Earth and Planetary Sciences, University of California Santa Cruz, 1156 High St, Santa Cruz, CA 95064 (U.S.A.)*
[*] *Corresponding Author Email Address: grobucho@ucsc.edu*

Abstract

Determining whether or not Pluto possesses, or once possessed, a subsurface ocean is crucial to understanding its astrobiological potential. In this study we use a 3D convection model to investigate Pluto's thermal and spin evolution, and the present-day observational consequences of different evolutionary pathways. We test the sensitivity of our model results to different initial temperature profiles, initial spin periods, silicate potassium concentrations and ice reference viscosities. The ice reference viscosity is the primary factor controlling whether or not an ocean develops and whether that ocean survives to the present day. In most of our models present-day Pluto consists of a convective ice shell without an ocean. However if the reference viscosity is higher than 5×10^{15} Pa s, the shell will be conductive and an ocean should be present. For the nominal potassium concentration the present-day ocean and conductive shell thickness are both about 165 km; in conductive cases an ocean will be present unless the potassium content of the silicate mantle is less than 10% of its nominal value. If Pluto never developed an ocean, predominantly extensional surface tectonics should result, and a fossil rotational bulge will be present if convection is not too vigorous. For the cases

which possess, or once possessed, an ocean, no fossil bulge should exist. A present-day ocean implies that compressional surface stresses should dominate, perhaps with minor recent extension. An ocean that formed and then re-froze should result in a roughly equal balance between (older) compressional and (younger) extensional features. These predictions may be tested by the *New Horizons* mission.
Keywords: Pluto, Thermal histories, Pluto, surface, Rotational dynamics

1. Introduction

The Pluto-Charon system is one of the least well understood in our Solar System. The present-day state of knowledge for Pluto is similar to that which existed for the icy satellites before spacecraft arrived in the neighborhood of Jupiter or Saturn. Interest in Kuiper Belt objects (KBO's) has grown due to the discovery of several bodies as big as Pluto in the last decade (e.g. Bertoldi et al., 2006). If it is possible to have a subsurface ocean inside a KBO, the total mass of liquid available today will be comparable to the mass of the Earth's oceans (Desch et al., 2009). It is therefore of considerable astrobiological (Mottl et al., 2007) and geophysical (Schubert et al., 2010) interest to determine the conditions under which Pluto may retain an ocean. Furthermore, in light of the forthcoming *New Horizons* results, it is important to investigate whether surface observations can be used to determine whether or not such an ocean exists. One of the main conclusions of this work is that there are several surface observations which may be used to infer the presence or absence of a subsurface ocean.

Our current knowledge of Pluto comes primarily from Earth-based remote

sensing. The heliocentric orbital parameters (Malhotra and Williams, 1997) and the Charon-Pluto orbit (Dobrovolskis et al., 1997) are well known. Direct observation during special events like the occultation of a star or by other bodies can provide information about the atmosphere (e.g. Elliot et al., 1989; Tholen and Buie, 1990; Pasachoff et al., 2005). Direct imaging of Pluto can also furnish some constraints on the Charon/Pluto mass ratio (Null and Owen, 1996) and the surface composition (Cruikshank et al., 1976; Owen et al., 1993). Direct imaging also gives us some information about the surface (Albrecht et al., 1994) and detected two new satellites around Pluto (Weaver et al., 2006; Buie et al., 2006). But these methods are insufficient to give us direct information about the internal structure of Pluto.

Nevertheless, Pluto is a body very similar to the better-known icy satellites of the giant planets. These satellites are mixtures of rock and ice and in some cases possess a subsurface ocean (see Hussmann et al. (2006) for a review) and resurfacing processes. Thus, it is reasonable to assume the same range of rheological proprieties and compositions for Pluto (McKinnon et al., 2008). Pluto's ice/rock+ice ratio is supposed to be about 0.65 (McKinnon et al., 1997) and for a differentiated Pluto the silicate core would be roughly 40% of the volume. The radiogenic heating provided by the core can potentially melt the mantle ice and form a subsurface ocean (Hussmann et al., 2006; McKinnon, 2006). The present-day spin period of Pluto and Charon reveals a system which is mutually synchronous, the stable end state of tidal evolution (Dobrovolskis et al., 1997). The energy dissipated in reaching this state provides Pluto with another heat source and can help to form a subsurface ocean (Collins and Barr, 2008). Finally, the presence of other volatiles such

as methane and ammonia can significantly reduce the melting temperature of ice (Grasset and Pargamin, 2005).

Previous investigations of the thermal evolution of Pluto have either assumed a conductive ice shell, or employed parameterized convection models (McKinnon et al., 1997; Hussmann et al., 2006; Desch et al., 2009). Here we employ the 3D numerical model OEDIPUS (Choblet, 2005; Choblet et al., 2007) to examine the behaviour of convective and conductive ice shells. Our model also includes a conductive silicate core, and tracks both spin and shape evolution. One major caveat is that we do not examine the effects of volatiles such as ammonia. As discussed below (Section 4), neglect of ammonia means that our results are conservative, in that the presence of NH_3 will permit an ocean to form and persist more readily. In the following section, we describe our model. In section 3 the results are presented and are further discussed in section 4.

2. Model

2.1. Structure and initial conditions

The parameters used in this study are listed in Table B.1. The mass measurements of Pluto and Charon have been improved during the last decade; the masses are now known to within 0.5% and 5% respectively (McKinnon et al., 2008). Olkin et al. (2003) give an estimate of the Charon-to-Pluto mass ratio of 0.122 ± 0.008, while Buie et al. (2006) give 0.1165 ± 0.0055. An orbital period P_{orb} = 6.38726 ± 0.00007 days, and semi-major axis of Charon's orbit, a = 19705 ± 8 km are given by Dobrovolskis et al. (1997) and very similar values are given by Buie et al. (2006) (P_{orb} = 6.3872304 ±

0.0000011 days and $a = 19571.4 \pm 4$ km). The radius of Pluto remains uncertain but based on occultations (Elliot et al., 1989; Pasachoff et al., 2005; Elliot et al., 2007), a range of values from 1158 to 1184 km has been suggested (Elliot et al., 2007). Following McKinnon et al. (1997), we assume an average radius, R, of 1180 km and an average density, ρ_0, of 1850 kg m^{-3} suggesting that the dwarf planet is composed of water ice and silicates. As in previous studies (McKinnon et al., 1997; Hussmann et al., 2006; Schubert et al., 2010), we suppose that the interior is differentiated into a silicate core and icy mantle (cf. Figure B.1a). Assuming an ice density of 950 kg m^{-3}, we obtain a core radius, R_c, of 849.6 km and a silicate density, ρ_{sil}, of 3361 kg m^{-3}. For simplicity, in the thermal evolution calculations, the average radius is assumed to remain constant.

The initial temperature profile of a satellite depends on the rate of accretion, and the timing of accretion relative to the decay of short-lived radionuclides (e.g. Schubert et al., 1981; Ellsworth and Schubert, 1983). Pluto is expected to have accreted slowly, perhaps between 20 million years (Kenyon, 2002) and a few hundred million years (Stern and Colwell, 1997) after the CAIs (Calcium-Aluminum-rich Inclusions) were formed at 4.567 Ga (Amelin et al., 2002). We assume that the accretion process is complete 30 Myr after CAI formation, in which case the short-lived radionuclides are not relevant. Following McKinnon et al. (1997), the surface temperature T_{surf} is set to 40 K and is kept constant throughout the simulation. This temperature is the expected N_2 surface-ice temperature (Elliot et al., 2007).

For simplicity, we assume that Pluto has an initially homogeneous interior temperature, and we test three different values: cold (150 K), intermediate

(200 K) and hot (250 K). There are two reasons for making such a simple assumption. First, the energy associated with Pluto's accretion is small compared to the long-term release of radiogenic heat (see below). Second, we do not anticipate that the initial temperature will greatly influence Pluto's long-term thermal evolution, which is our primary interest. As we demonstrate below (Section 3.2), as expected, the effect of the initial temperature does not significantly change the final results. This assumption is also conservative, in that it does not assume that an ocean is initially present.

2.2. Heat sources

The thermal history of Pluto depends on the different heat sources available during its evolution (Table B.2). The first is the energy associated with the accretion of Pluto. If all the energy associated with accretion were converted to heat, a primordial ocean would result. However, in practice much of the heat is liable to be lost promptly to space via radiation, resulting in less warming (e.g. Schubert et al., 1981; Ellsworth and Schubert, 1983; Hussmann et al., 2010). Differentiation of Pluto, assuming it occurred, contributes a small additional heating term (Hussmann et al., 2010). The formation of Charon does not generated significant global heating (McKinnon, 1989), although the impact zone might have undergone a temperature increase of $\approx$ 150 K (Canup, 2005). Nevertheless, Charon causes Pluto to slow down its spin period. This despinning is another energy source which will be released within Pluto in a very short time, of order 10^5 years (Hussmann et al., 2010).

However, the main source of energy within Pluto is the radioactive decay of long-lived isotopes contained in the silicate core (one order of magnitude

larger than the other heat sources (cf. Table B.2)). Owing to the assumed time of the end of the accretion process, the short-lived isotopes do not contribute significantly. We assume a silicate composition corresponding to carbonaceous chondrites following Lodders (2003) (cf. Table B.3). Other assumed compositions would contribute somewhat different heat budgets (see below). Among the different elements, potassium is the most important contributor, and is also the most uncertain in abundance, owing to its volatility. Below we investigate the influence of a range of potassium concentrations on the evolution of Pluto.

2.3. Dynamics

2.3.1. Ice shell

The internal dynamics of Pluto's ice shell are studied in a 3-D spherical shell assuming the material behaves as an infinite Prandtl number fluid. The classical conservation equations for thermal convection (mass, momentum and energy) are considered in the Boussinesq approximation with a viscosity that strongly depends on temperature and is solved using the numerical tool OEDIPUS (Choblet, 2005; Choblet et al., 2007). This code uses the "cubic sphere" coordinates introduced by Ronchi et al. (1996). OEDIPUS uses a multigrid solver to solve the conservation equations of momentum and mass, and typically does so in parallel using the MPI library. Further details about the numerical procedure can be found in Choblet (2005) and Choblet et al. (2007). The whole spherical shell is divided into six identical blocks. In the present study, only one of the six blocks is used to model Pluto's internal dynamics. The numerical domain, when we begin, is bounded by an internal sphere corresponding to 72 % of Pluto's radius, that is a core radius of 849.6

km. A temperature based on the core temperature evolution (see below) is prescribed at the inner boundary. Gravity g is a function of radius r: $g(r) = \frac{4\pi}{3} G\rho_0 r$, corresponding to a surface value g_s of 0.61 m s^{-2}.

The three conservation equations (mass (Eq. 1), momentum (Eq. 2), and energy (Eq. 3)) governing mantle convection solved in OEDIPUS are, in dimensionless form:

$$\nabla.\mathbf{v} = 0 \tag{1}$$

$$0 = -\nabla p + \nabla.(\eta(\nabla\mathbf{v} + (\nabla\mathbf{v})^t)) + \mathbf{f} \tag{2}$$

$$\frac{DT}{Dt} = \nabla^2 T + H \tag{3}$$

with velocity $\mathbf{v}$, pressure p, viscosity η , temperature T, time t, buoyancy force $\mathbf{f}$ and H volumetric heating rate. Superscript ^{t} denotes the transpose of the second order tensor. OEDIPUS is a finite volume program based on the "cubed sphere" non-conformal coordinate system (r, ξ, η). The above equations are solved in their dimensionless form, where the following classical characteristic scales have been adopted: $d = 330$ km, average Pluto ice shell thickness for length ; $\Delta T = T_m - T_{surf}$ for temperature difference (with T_{surf} the surface temperature and T_m the melting temperature of pure water ice); and $\tau = R^2/\kappa_m$, diffusive scale for time (with κ_m the thermal diffusivity at T_m and R the radius of Pluto).

The vigor of convection is governed by the Rayleigh number, Ra, which we evaluate at the base of the ice shell:

$$Ra = \frac{\alpha_b \ \rho_{ice} \ g \ (T_b - T_{surf}) \ d^3}{\kappa_b \ \eta_b} \tag{4}$$

Here all variables are computed at the temperature T_b at the base of the ice shell: α is the thermal expansivity, ρ_{ice} ice density, g acceleration due to the

gravity, d ice shell thickness and κ thermal diffusivity. The values of these parameters are given in Table B.1. Further details about the treatment of viscosity and benchmarking of the OEDIPUS code are given in Appendix B.

In the majority of our calculations, the grid mesh contained $32 \times 64 \times 64$ cells (in r, ξ and η, respectively). To check for resolution issues, in a few low-viscosity runs we used a higher resolution (grid mesh = $64 \times 128 \times 128$ cells) and verified that the results were indistinguishable from those carried out at lower resolution.

2.3.2. Core

We assume that the silicate core is sufficiently cold that heat is transferred by conduction. The thermal evolution of the core is determined using a numerical program initially written by Tobie and Cecconi (2000) and modified for this study. This conduction code uses a spherical geometry and the equation is solved radially (1D code) with a predictor-corrector method. At the beginning of the evolution, the numerical domain extends from the center of Pluto to the core-mantle boundary (CMB). The mesh size is set to half the initial radial mesh size of OEDIPUS ($\Delta r_2 = \Delta r_1/2$, see Fig. B.1a).

The equation solved is the energy equation (Eq. 3) but without the velocity terms. Thus the equation is :

$$\rho C_p \frac{dT}{dt} = \nabla \cdot (k \cdot \nabla T) + H \tag{5}$$

with k the thermal conductivity. This equation and all the variables in the conduction code are used in their dimensionalized form. We checked the code output against the analytical solution given by Carslaw and Jaeger (1959).

In the absence of an ocean, the two codes are coupled by having a common temperature at the silicate-ice interface. When an ocean separates the silicates from the ice shell, the temperature at the silicate surface is set to the ice melting temperature T_m and the heat flux out of the core is transferred directly to the base of the ice shell (see below). We make this assumption because the low viscosity of water will result in vigorous convection and thus efficient heat transfer across the ocean. Note that we neglect the adiabatic temperature increase across the ocean due to the low gravity and small coefficient of thermal expansion (2.12×10^{-4} K^{-1} at 293 K (Tanaka et al., 2001)). Such a small coefficient gives only ~ 1 K of temperature increase for an ocean 200 km thick.

2.4. Melt and rheology

2.4.1. Melt

The heat conducted out of the silicate core may result in melting of the overlying ice. At the top of the core ($r = R_c$), the heat flux is F_c. Since this heat is assumed to be transferred efficiently through the ocean, the heat flux at the base of the ice shell is $F_c' \approx F_c \left(\frac{R_c}{R_{j-1}}\right)^2$, where R_{j-1} is the radial cell location at base of the shell (see Fig. B.1b). For this particular cell, the rate of change of energy may be approximated as follows:

$$\frac{\Delta E}{\Delta t} = F_c' A_{j-1} - k \frac{T_j - T_{j+1}}{\Delta r_1} A_j \tag{6}$$

where the first term on the RHS is the energy input from the ocean below, the second term is the conductive heat transfer upwards, k is the thermal conductivity and T_j and A_j are the temperature and cross-sectional area of cell j (see Fig. B.1b). The melt fraction in this cell is f_m. Assuming that

melting has already started (i.e. that $f_m > 0$) then T_j is pinned at the melting temperature T_m and the net change in energy is responsible for melting or freezing, that is, an increase or decrease in f_m:

$$\Delta f_m = \frac{\Delta E}{\rho_{ice} V_j L_a} \tag{7}$$

where V_j is the volume of that particular cell, ρ_{ice} is the ice density and L_a is the latent heat of ice. In our implementation, tracking melting and freezing requires the boundary between the 1D and 3D code to change with time. Further details of the technique employed are given in Appendix A, including comparison with analytical solutions to verify that both the melting and freezing calculations are being performed correctly.

2.4.2. Rheology

An Arrhenius law is assumed to describe the temperature dependence of the viscosity $\eta(T)$ inside the icy mantle:

$$\eta(T) = \eta_m \exp\left(\frac{E_a}{\mathcal{R}}\left(\frac{1}{T} - \frac{1}{T_m}\right)\right) \exp\left(f_m \gamma_m\right) \tag{8}$$

with $T_m = 273$ K and $\eta_m = \eta(T_m) = 10^{13} - 4.16 \times 10^{17}$ Pa s, the reference temperature and viscosity, $E_a = 60$ kJ mol^{-1} the activation energy, γ_m a dimensionless constant and $\mathcal{R}$ the gas constant. Note that the reference viscosity is defined at 273 K and thus depends on factors such as grain size and composition, but not temperature. For numerical reasons, a cut-off is prescribed for the viscosity function (see Appendix B): $\eta = \min(\eta(T), 1.2 \times 10^6\ \eta_b)$ where η_b is the viscosity at the bottom of the ice shell T_b. We add a melt dependence through the γ_m coefficient. Following De La Chapelle et al. (1999), a melt fraction of 5% induces one order of magnitude decrease of the ice viscosity, so γ_m is set to 45.

2.5. Rotational dynamics and dissipation

The evolution of Pluto cannot be studied without taking into account the formation of its satellite Charon. It is likely that this formation occurred early (within a few hundred million years after CAI formation) but the actual time is unknown. We set the formation of Charon at 100 Myr after the end of Pluto's accretion, or 130 Myr after CAI formation. Initially, Pluto and Charon probably had a rotation period of only a few hours (Lissauer and Safronov, 1991; Canup, 2005). The misalignment of Pluto's tidal bulge with respect to Charon acted as a torque that tended to slow down the spin. This torque on Pluto is given by (e.g. Peale, 1999):

$$T = \frac{3}{2}\frac{k_2(t,\chi)GM_c^2R^5}{a(t)^6Q(t,\chi)} \tag{9}$$

with k_2 the tidal Love number and Q^{-1} the specific dissipation function both computed at the average tidal frequency $\chi = 2(\omega - n)$ where ω is the spin rate and n is the orbital mean motion (Efroimsky and Williams, 2009); G the universal constant of gravity, M_c Charon's mass, R Pluto average radius and a the semi-major axis of the orbit. In our case, the angular momentum associated with the initial spin has the same order of magnitude as the one due to the orbit. Thus, we have to conserve angular momentum in order to determine the evolution of the semi-major axis (Dobrovolskis et al., 1997). This conservation is given by (e.g. Murray and Dermott, 1999):

$$L = I\omega + \frac{M_pM_c}{(M_p + M_c)}a^2n \tag{10}$$

with I the moment of inertia of Pluto and M_p and M_c respectively the mass of Pluto and Charon. Note that here we are neglecting Charon's spin. We

assume a two-layer Pluto structure (Fig B.1a) to compute the moment of inertia. The gradual decrease of the spin rate ω and the increase of the semi-major axis as a function of time t are then determined from the tidal torque acting on Pluto (Eq. 9) and the conservation of angular momentum (Eq. 10):

$$\frac{d\omega}{dt} = \text{sign}(n-\omega)\ \frac{3}{2}\frac{k_2(t,\chi)GM_c^2R^5}{a(t)^6Q(t,\chi)I} \tag{11}$$

$$\frac{da}{dt} = \text{sign}(\omega-n)\ \frac{3k_2(t,\chi)}{Q(t,\chi)}\frac{M_c}{M_p}\left(\frac{R}{a}\right)^5 an \tag{12}$$

We used two different viscoelastic linear rheologies to calculate k_2 and Q: a Maxwell model and a Burgers model.

Both models are often used for computing tidal heating in icy bodies (e.g. Moore and Schubert, 2000; Hussmann et al., 2002; Robuchon et al., 2010). The Maxwell model is the simplest physically reasonable description of dissipation in solids. However, it does not reproduce the experimentally-observed frequency-dependence of dissipation in materials (Sotin et al., 2009). More complex models, based on laboratory measurements (Tatibouet et al., 1986; Cole, 1995) or on analysis of tidal bending of polar glaciers (Reeh et al., 2003), are probably more appropriate for describing the viscoelastic response across a wide range of temperatures and frequencies, but require more parameters to be specified. The advantage of the Maxwell model is that it depends on only two parameters that can be experimentally derived: an elastic shear modulus, μ, and a long-term viscosity, η. This long-term viscosity thus corresponds to the convective viscosity (Eq. 8). The Burgers model includes a secondary dissipation peak at low temperatures. It is described by a transient shear modulus, μ_B , and a short term viscosity, η_B , in addition to the

two Maxwell parameters. For simplicity, we assume $\mu_B = \mu$ as proposed by Reeh et al. (2003). In our nominal model we assume a Burgers rheology and take $\eta/\eta_B = 50$ following Robuchon et al. (2010). We examine the sensitivity of our results to this assumption in Section 4.1.

The energy associated with despinning is assumed to partition into the ice shell, depending on the local viscosity η. Following the approach of Roberts and Nimmo (2008), the local heating rate is scaled by the dimensionless parameter H_f, given by:

$$H_f = \left(\frac{\omega\eta/\mu_{ice}}{1 + (\omega\eta/\mu_{ice})^2} \right) / \left(\frac{\omega\eta_m/\mu_{ice}}{1 + (\omega\eta_m/\mu_{ice})^2} \right) \tag{13}$$

where μ_{ice} is the shear modulus of the ice and η_m the reference viscosity.

2.6. Surface stress and flattening

During its global evolution, Pluto's average temperature changes and can cause an increase or decrease of its volume. If a liquid layer appears, the phase transition of the ice also causes a change in volume. These different volume variations induce surface stresses. For each time step, we compute the temperature variation and the water volume which appears or disappears in order to obtain the surface stress evolution.
The volume change induced by the temperature is:

$$\Delta V_T(t) = -V\alpha \left(T(t) - T(t-1) \right) \tag{14}$$

with V the volume associated with the mesh point, α the thermal expansivity of ice or silicate and $T(t)$ and $T(t-1)$ respectively the temperature at the time t and $t-1$. In the same way, the volume variation due to the ice phase

transition is:

$$\Delta V_{iw}(t) = -V\left(1 - \frac{\rho_{ice}}{\rho_{wat}}\right)\left(f_m(t) - f_m(t-1)\right) \tag{15}$$

with $f_m(t)$ and $f_m(t-1)$ respectively the melt fraction at the time t and $t-1$ and ρ_{wat} the water density. Both volume changes induce a radius variation of Pluto which can be evaluated by:

$$\Delta R = R - \left(R^3 - \frac{\Delta V_T + \Delta V_{iw}}{\frac{4}{3}\pi}\right)^{\frac{1}{3}} \tag{16}$$

where ΔV_T and ΔV_{iw} are the contributions from the radially-integrated effects of temperature and melting/freezing. Assuming that the near-surface ice responds in an elastic fashion, the corresponding stresses are (Melosh, 1977):

$$\sigma_s = 2\mu_{ice}\left(\frac{1+\nu}{1-\nu}\right)\frac{\Delta R}{R} \tag{17}$$

with μ_{ice} and ν respectively the shear modulus and Poisson ratio of the ice. The Poisson ratio is taken to be 0.5 because we assume an incompressible case.

In order to determine the evolution of the flattening as the satellite despins, we compute the time evolution of the second-degree surface displacement using a spectral technique already used by other studies (Čadek, 2003; Tobie et al., 2008; Robuchon et al., 2010). The satellite is assumed to behave as an incompressible Maxwell-type viscoelastic body. An ocean, if present, is treated as a low-viscosity, low-rigidity layer rather than as an inviscid fluid. This approximation is acceptable as long as the Maxwell time of the ocean is not close to the forcing orbital period. The body force includes the centrifugal force and self-gravitation due to mass redistribution (Čadek, 2003).

We start our simulations from a stress-free initial state and then impose the centrifugal force. We compute the evolution of the surface displacement from the (time-dependent) radial viscosity profile, given by OEDIPUS, at the corresponding spin rate. Unlike the thermal convection calculations, no viscosity cut-off is prescribed, so that the viscosity can reach values as high as 10^{80} Pa s at the surface (effectively elastic).

3. Results

Each simulation is in two steps: (1) we first compute the coupled thermal evolution and despinning and (2) we then use the evolution of both viscosity profile and rotational period in order to evaluate the flattening of Pluto.

3.1. Thermal evolution

Figure B.2 shows two possible thermal evolution scenarios for Pluto: one with a low reference viscosity (10^{13} Pa s) in which ice shell convection occurs (Figs. B.2a-d), and another with a higher reference viscosity (4.16×10^{17} Pa s) in which convection never develops (Figs. B.2e-h). Both cases start with an assumed uniform temperature of 150 K; only the case with a high reference viscosity develops an ocean, which persists to the present day. In the low reference viscosity case, vigorous convection develops and the ice shell never melts.

3.1.1. Ocean evolution controlled by convection and conduction

Figs B.2a and B.2e depict the evolution of laterally-averaged temperature with time in both the silicate core and ice shell. In both cases the main effect is the warming of the core due to radioactive decay. The silicates warm up

the overlying ice shell, which accordingly becomes more dissipative.

The crucial difference between the two cases is that in Fig. B.2a (lower reference viscosity), as the ice shell warms up, convection occurs, starting at 101 Myr. This convection increases the heat flux across the ice shell to about ~ 2 mW m^{-2} (black line in Fig B.2b) and is sufficient to transfer the heat being conducted out of the silicates to the surface. As a result, the ice shell remains solid. Conversely, in Fig. B.2e the viscosity is too high for convection to happen. The conductive shell is not able to transfer the heat from the underlying silicates rapidly enough to avoid melting (McKinnon, 2006). As a result, an ocean begins to form at around 232 Myr and grows until the silicate heat flux is balanced by heat conducted across the floating ice shell.

The peak silicate heat flux (≈ 5 mW m^{-2} evaluated at the surface) occurs at around 1 Byr (red line in Fig B.2b and B.2f). In the low viscosity case (Fig B.2a) convection is sufficient to transfer this heat from the core; as a result, no melting occurs throughout the thermal evolution. In detail, a conductive (stagnant) lid ~ 100 km thick caps a convecting icy mantle ~ 230 km thick. The convective region is characterized by an isothermal temperature of ~ 230 K and the CMB temperature reaches a maximum of 250 K at about 1.2 Byr when the CMB heat flux reaches its peak. As the CMB temperature increases, the basal viscosity of the ice shell decreases and the convective heat flux increases. In this way a rough balance between the CMB heat flux and the convective heat flux is maintained (Fig B.2b) , and the CMB temperature never reaches the melting point of ice.

By contrast, in the high viscosity case (Fig B.2e), the conductive shell thins

to a minimum thickness of 100 km at 1.2 Byr, at which point the heat from the core balances the heat conducted across the shell (Fig B.2f) . As the core heat flux subsequently declines, the shell thickens conductively. The rate of refreezing is relatively slow and as a result, the ocean persists to the present day, consisting of 165 km of liquid beneath 165 km of ice.

3.1.2. Despinning

This picture is not fundamentally changed by despinning. As Pluto spins down, the despinning energy is deposited mainly at the base of the ice shell, where the ice viscosity is lowest. This process causes a spike in the temperature shortly after Charon's assumed formation time of 100 My in both cases (Figs B.2a and B.2e). Figs B.2d and B.2h show the evolution of spin rate with time (black line), and demonstrate that once the ice shell becomes warm enough, synchronous rotation is achieved rapidly - within a few Myr. This is because of the feedback between local dissipation due to despinning,and the consequence of warming of the ice. The despinning energy deposited within the ice shell is relatively small compared to other heat sources but can still melt a few tens of kilometers of ice (Table B.2). As a result of this rapid despinning transient, a negative heat flux (see Fig. B.2b and B.2f) appears at the CMB because the shell is warmed up faster than the core. Once synchronous rotation is acquired, any melt produced freezes in a few tens of millions years and this energy is absorbed both by the core and ice shell. Comparisons between the above cases and identical cases without despinning show that the impact of this process on the thermal evolution is small. As the despinning energy is small compared to the radioactive energy, once the ocean begins to form, the thermal evidence of despinning is erased. Note,

however, that the stresses associated with despinning may be significant (see below).

3.2. Role of the reference viscosity and initial temperature

The propensity of an ice shell to convect depends on the viscosity at the base of the shell, and the shell geometry (see Appendix B). In our model runs we find that changing the reference viscosity or the initial temperature changes the thermal evolution. Table B.4 summarizes the outcomes of different combinations of initial temperature and reference viscosity. Figure B.3 depicts results for this same range of reference viscosities and initial temperatures respectively for the RMS (Root Mean Square) velocity, ocean thickness, surface heat flux and surface stress. These figures show groups of columns with each group representing one reference viscosity (from the left to the right : 10^{13} Pa s, 10^{14} Pa s, 10^{15} Pa s, 4.16×10^{15} Pa s, 4.16×10^{16} Pa s and 4.16×10^{17} Pa s). Except for the lowest-viscosity case, groups consist of three different initial temperatures: (left: 150 K, center: 200 K and right: 250 K).

In all our simulations with a reference viscosity $\leqslant 4.16 \times 10^{15}$ Pa s convection occurs whatever the initial temperature (Fig. B.3a). In cases with an initial temperature of 150 and 200 K convection starts after the despinning produces high temperatures close to the CMB. For an initial temperature of 250 K convection can start before despinning. In none of these cases do we obtain an ocean at the present-day (Fig. B.3b), and with a reference viscosity $\leqslant 10^{15}$ Pa s, convection is vigorous enough that an ocean never forms at all. The case with a reference viscosity of 4.16×10^{15} Pa s is intermediate, in that an ocean forms and then partially re-freezes. Initially convection is not

vigorous enough to avoid melting of the ice shell. However, as the shell thins, the convective vigor decreases and stops. Subsequently, as the the heat flux from the core begins to decrease, the ocean begins to freeze and the conductive ice shell thickens. At the present-day the shell remains conductive and the present-day state resembles those of purely conductive cases.

As we increase the reference viscosity to 4.16×10^{16} Pa s, convection can still occur (Fig. B.3a). For convection to take place, we need a thick ice shell and temperatures close to the melting temperature near the CMB. These conditions are not met with an initial temperature of 150 K and 200 K, but with an initial temperature of 250 K, convection does initiate. The sluggish heat transfer, however, results in relatively prompt ocean formation (Fig. B.3b) and the cessation of convection shortly thereafter. The subsequent thermal evolution in these three cases is identical irrespective of the initial temperature, because the ice shell is conductive. At the present-day, we obtain an ocean thickness of 165 km (Fig. B.3b) and a surface heat flux of ~ 2.8 mW m^{-2} (Fig. B.3c).

Our highest reference viscosity (4.16×10^{17} Pa s) does not allow convective motion at all (Fig. B.3a). The only differences between scenarios with different initial temperature are the time needed to obtain the current spin period and the time when the ocean begins to form.

The surface heat flux (Fig. B.3c) is mainly controlled by the vigor of the convection; the present-day heat flux (Table B.4) increases slightly with increasing reference viscosity, because of the increased time it takes to respond to changes in the basal heat flux.

In summary, Figures B.3a-B.3c show that the initial temperature is not very

important in determining Pluto's long-term thermal evolution. The reason for this is that Pluto's energy budget is likely dominated by silicate radiogenic heat production (see Table B.2). On the other hand, the reference viscosity is crucial, because it controls whether or not convection occurs, and whether an ocean exists at the present day (Table B.4).

3.3. Role of Potassium

The results above show that the present-day state of Pluto is controlled mainly by silicate decay of the radioactive elements. Among these isotopes, potassium provides the main contribution to the heat budget and is most uncertain in abundance (because of its volatility). Thus, we performed 3 further simulations with different potassium contents (50, 200 and 400 ppb, compared to the reference value of 738 ppb, see Table B.3) in order to investigate its impact on the thermal evolution. Because we are interested the circumstances under which an ocean will occur, we assumed a conductive case with a reference viscosity of 4.16×10^{16} Pa s and an initial temperature of 150 K to maximize the likely ocean lifetime.

With 400 ppb of potassium, the despinning process is delayed to 297 Myr compared to 195 Myr with the nominal content in potassium. No convection occurs throughout the thermal evolution due to the high reference viscosity. An ocean begins to form at 440 Myr, and at the present day, the ocean thickness is $\sim$ 114 km and the shell is conductive.

The case with 200 ppb show similar behavior. But, owing to the smaller amount of potassium, the onset times of other various processes are delayed: despinning occurs at 496 Myr and an ocean begins to form at 815 Myr. Even with this small potassium content an ocean will still be present now (thick-

ness of 57 km beneath a conductive shell).

Finally, with 50 ppb, no ocean appears. Pluto acquires its present-day rotational period at 1.163 Byr and convection never initiates.

Thus, to avoid an ocean forming if the shell is conductive, a potassium content $< 10\%$ of the reference value is required. But even with these small quantities we always reach the present-day spin period. This is due to the high temperatures (close to the melting temperature) reached in every case, close to the CMB.

3.4. Constraints on shape and surface stresses

An important observable parameter is the shape of Pluto, in particular whether or not it can sustain a fossil (rotational) bulge from an earlier epoch. That depends on its thermal and spin evolution.

Figure B.4 shows the time evolution of the rotational flattening for three cases with an initial temperature of 150 K: a cold case with [K] = 50 ppb and $\eta(T_m) = 10^{14}$ Pa s, a second one with the nominal content of potassium ([K] = 738 ppb) and $\eta(T_m) = 10^{15}$ Pa s and a final one with the nominal potassium content and a higher $\eta(T_m) = 4.16 \times 10^{16}$ Pa s. In the first two cases (Fig. B.4a and Fig. B.4b)) no ocean develops, and for the third case (Fig. B.4c) the ice shell starts to melt at about 185 Myr. Here the red line is the model flattening, while the green line is the flattening which would be obtained if Pluto were a purely fluid body (no fossil bulge). The latter was calculated using the Darwin-Radau approximation (e.g. Murray and Dermott, 1999). In all cases, the model flattening decreases significantly when despinning occurs, as expected. However, in general the model flattening does not immediately reach the value (≈ 0) predicted by the purely fluid

assumption. This is because the near-surface of Pluto is relatively viscous and deforms slowly. The no-ocean cases (Fig. B.4a and B.4b) show different behavior. The present-day shape for the low potassium content case (Fig. B.4a) is significantly different from the expected fluid value and implies an observable fossil bulge (flattening ≈ 0.0058). This is because the bulk of the shell remains cold and rigid throughout Pluto's thermal evolution. For the case with convection (Fig. B.4b), by contrast, the present-day shape is approximately that expected for a fluid body. This is because the lower-viscosity convecting ice shell has had time to relax to its equilibrium shape. Finally, in the case with an ocean (Fig. B.4c), the shape reaches the expected fluid value as soon as the overlying shell becomes sufficiently thin. The significance of this result is that, if *New Horizons* measures a fossil bulge, it strongly implies both the absence of a subsurface ocean and the presence of a conductive or sluggishly convecting lid.

Whether or not an ocean forms has important implications for surface tectonics. Figures B.2c and B.2g plot the surface stresses due to volume change as a function of time (Section 2.6). In both cases, minor initial contraction is followed by significant expansion as the ice and silicates warm up. If no ocean develops (Fig. B.2c), this expansion slows and then reverses as the body starts to cool. The net effect at the present day is a function of the initial temperature: large ($\approx$ + 18 MPa) extensional stresses if the initial temperature is low, and smaller ($\approx$ - 9 MPa) compressional stresses if the initial temperature is high. Conversely, if an ocean develops, as in Fig. B.2g, the conversion of low-density ice to higher-density water results in contraction and large compressional stresses. As the ocean subsequently

re-freezes, extension occurs. If the ocean does not freeze completely (Fig. B.2g), the net stresses are still large ($\approx$ - 30 to - 70 MPa) and compressional at the present day (see also Fig. B.3d).

In cases where the ocean freezes completely, the final stress state depends on the initial temperature. A higher initial temperature gives larger net compressional stresses at the present-day than a low initial temperature (Fig. B.3d).

Cases with a present-day ocean are associated with net compressional stresses. If an ocean never formed, net stresses of either sign can result, although extensional stresses are more likely (Fig. B.3d). In either case, these volume-change stresses greatly exceed likely present-day stresses due to any non-synchronous rotation (Collins and Pappalardo, 2000).

The above analysis assumes that the stresses are cumulative, and are not relaxed by brittle failure or plastic flow. This assumption is highly idealized; in reality, the shell is likely to fail and then anneal, recording successive episodes of deformation. Thus, ocean formation followed by partial ocean re-freezing will result in older compressional features overlain by later extensional features. In cases with a present-day ocean, the ratio of extension- to compression-accommodating features should be lower than in cases without a present-day ocean. Cases which never formed an ocean will show older extensional and younger compressional features.

This picture is complicated somewhat by the despinning stresses, which are shown in Figs B.2d and B.2h as the red line. The magnitude of these stresses is comparable to those caused by volume changes, but the former are compressional at the equator and extensional at the poles (Melosh, 1977)

while the latter are isotropic. The resulting stress and tectonic feature pattern will therefore be somewhat complex; nonetheless, the key point is that bodies with and without oceans should develop rather different patterns of tectonic features.

4. Discussion and comments

Since Pluto belongs to the Kuiper belt, the coldest region of our Solar System, it is striking that some of our models predict a present-day ocean. This result agrees with the conclusions of most previous studies of Pluto (McKinnon et al., 1997; Schubert et al., 2010) and large KBOs (Hussmann et al., 2006; McKinnon et al., 2008; Desch et al., 2009). Our results show that for reference viscosities $\geq 4.16 \times 10^{15}$ Pa s Pluto is likely to have a present-day ocean (unles the potassium concentrations are $\leq$50 ppm) and a conductive ice shell. If the reference viscosity is lower and the ice shell is convective, no ocean will be present.

With no present-day ocean, we predict post-despinning tectonics that are predominantly extensional (perhaps with recent compression), and the possibility of a large fossil bulge. If an ocean forms tectonics are expected to be compressional (perhaps with recent extension) and a hydrostatic shape should be observed. These predictions are testable by the *New Horizons* mission.

4.1. Parameter Uncertainties

Many parameters are poorly known and may affect the outcome of our model results. The two most important are probably ice viscosity and radiogenic abundances. Most of the studies dealing with thermal evolution of

icy mantles have chosen a viscosity at the melting temperature of between 10^{13} Pa s and 10^{15} Pa s (Tobie et al., 2003; McKinnon, 2006; Roberts and Nimmo, 2008). We adopted an expanded range to mimic the effect of an increased viscosity due to colder oceans in the presence of NH_3 (see Section 4.2). More detailed approaches taking into account the feedback between viscosity and grain size (e.g. Barr and McKinnon, 2007) are outside the scope of the current work. Our assumption of a Newtonian viscosity (e.g. due to diffusion creep - (Duval et al., 1983; Goldsby and Kohlstedt, 2001)) is justified by the generally low stresses characteristic of convection.

As discussed in Section 2.1 the internal structure of Pluto is currently uncertain. In particular, the silicate mass fraction (which determines the core radius and radioactive heating) might range from 0.5 to 0.7 according to McKinnon et al. (1997), depending on the presence of different ice phases and/or organic material. This range results in a core radius changing by only 50 km. Such a small change will not have a large influence on our results, because the radioactive heating will change by only $\sim \pm$ 20%.

We also investigated whether our results are sensitive to a change of rheological model (Maxwell) or to different ratios of the long-term viscosity $\eta(T)$ over the short-term viscosity $\eta_B(T)$ for the Burgers model. Synchronous rotation is reached for all the models and parameters we investigated. These models are sensitive to the temperature and rotation period (e.g. Ojakangas and Stevenson, 1989; Reeh et al., 2003), with the temperature being the more important parameter. We find that the warming core allows the icy shell to reach the temperature needed to achieve despinning irrespective of the parameters or rheological model used.

We also performed two simulations with initial spin periods of 3 and 9 hours respectively and the nominal rheological parameters. Both simulations generated the present-day synchronous rotation rate. As in the previous cases, despinning occurs over an interval of roughly one million years for an initial period of 3h or 9h. Differences between the two cases are due to the second dissipation peak in the Burgers model which is reached at different times.

The radiogenic abundances also have a strong effect on the thermal evolution. We used radiogenic concentrations based on carbonaceous chondrites following Lodders (2003). Other assumed compositions might also be used, like ordinary chondrites or enstatite chondrites. Although we have some timing constraints on the formation of different kinds of chondrites (e.g. Kleine et al., 2009; Schulz et al., 2010), whether one of these compositions is relevant to the Kuiper Belt is currently unclear (Ciesla, 2010). The main contributor among the long-lived radioactive species is potassium, which may vary in concentration from 0 for a depleted model to more than 1000 ppb (ordinary chondrite for Castillo-Rogez et al. (2007)). Our assumed range of concentration goes from 50 ppb to 738 ppb. Higher values will make ocean formation easier and will not significantly change our conclusions.

Other minor complications have been neglected because they are unlikely to change the conclusions. For instance, the ice I-ice II phase transition occurs at about 220 MPa (Leliwa-Kopystynski et al., 2002), so some cases might result in a thin layer of ice II (cf. McKinnon et al., 1997). Similarly, the thermal conductivity of the ice shell is somewhat uncertain, since it may be affected by porosity (at shallow depths) and the presence of clathrates (Ross

and Kargel, 1998).

4.2. Ammonia

In this initial study, we have neglected the role of ammonia, which can have a profound effect on satellite evolution (e.g. Leliwa-Kopystynski et al., 2002; Spohn and Schubert, 2003; Tobie et al., 2006; Hussmann et al., 2006; Mitri and Showman, 2008; Stegman et al., 2009). The incorporation of few percent of ammonia depresses the melting point (Grasset and Pargamin, 2005) of water making the formation of a subsurface ocean easier. The concentration of NH_3 relative to H_2O in Pluto is probably 1-5 wt% according to Desch et al. (2009), although if complete nebular concentration of nitrogen occurred, this value could reach 15 wt% (Lunine and Stevenson, 1987; Mousis et al., 2002; Lodders, 2003). Ammonia could also lower the shell viscosity compared to pure water ice (Durham et al., 1993; Arakawa and Maeno, 1994), in the somewhat unlikely event that it is incorporated into the solid shell. Thus, although the presence of ammonia is most likely to increase the probability of Pluto having a present-day ocean, its effects are not entirely obvious, and will be the subject of future study.

4.3. Effect of an ocean

Our models show that under the assumption of high reference viscosities it is easy for Pluto to form a liquid ocean between a conductive ice shell and a silicate core. The presence of this ocean, in turn, implies physical changes at the interface with the core. Firstly, serpentinization of the silicate core (e.g. Ransford et al., 1981) may occur. This chemical reaction is exothermic, but the heat production remains very small compared to the radioactive heating

(0.02 % of radiogenic heating (Vance et al., 2007)). Other studies show that this process may change the thermal evolution of the core by removing potassium from the core (e.g. Shock and McKinnon, 1993; Castillo-Rogez and Lunine, 2010).

Although the two observables that we have focused on are surface tectonics and global shape (see above), there are two other interesting consequences of a subsurface ocean. First, the spin state of Pluto may be diagnostic of an interior fluid layer, as has recently been argued for the large satellite Titan based on its observed obliquity and gravity moments (Bills and Nimmo, 2011). Second, ocean refreezing not only leads to large extensional stresses within the ice shell (Nimmo, 2004) but also a pressurization of the ocean, which in some cases may lead to cryovolcanism (Manga and Wang, 2007). Resurfacing of some KBO's has been advocated based on the presence of crystalline ice (Jewitt and Luu, 2004; Cook et al., 2007). Images from *New Horizons* missions will be able to clarify this topic for Pluto.

5. Summary and perspectives

Our results may be summarized as follows. Whether or not Pluto develops an ocean depends on the rate of heat transfer across the ice shell compared with the heat produced by radiogenic elements (McKinnon, 2006). We find that, for the nominal potassium abundance, there is a critical reference viscosity above which an ocean develops. For reference viscosities in the range $10^{13} - 10^{15}$ Pa s vigorous convection occurs and an ocean never forms. For reference viscosities $\geq 4.16 \times 10^{15}$ Pa s, convection is either sluggish or absent, and present-day Pluto possesses an ocean of roughly 165 km thick-

ness beneath a conductive ice shell 165 km thick. If the core is sufficiently depleted in potassium, an ocean never forms irrespective of the reference viscosity. Without an ocean during Pluto's past, surface tectonics will be predominantly extensional (perhaps with minor recent compression) and a fossil bulge may be present. For cases which possess an ocean, there is no fossil bulge, and compressional surface stresses should dominate (perhaps with minor recent extension).

This study does not include the presence of volatiles such as ammonia, which are likely present and may have an effect on Pluto's thermal evolution. The main effect of incorporating ammonia is to produce colder ocean temperatures and thus generate ice shells which are more likely to be conductive. Ammonia thus increases the likelihood that Pluto currently possesses a subsurface ocean.

The broader implications of this work are twofold. First, whether icy bodies develop subsurface oceans is an important question from both an astrobiological (Mottl et al., 2007) and a geophysical (Schubert et al., 2010) point of view, and this study further illuminates which parameters are most important.

Second, and more importantly, our results demonstrate strong links between the presence or absence of an ocean, the behavior of the ice shell, and observable surface features. To the best of our knowledge, such links have not been proposed before for Pluto. Our results may thus be combined with images and topographic data returned by *New Horizons* to investigate whether or not Pluto has a subsurface ocean. If it does, then the outer edge of the potentially habitable zone of the Solar System will have suddenly expanded

from 10 AU (Saturn) to 40 AU.

Acknowledgments

Reviews by two anonymous referees were greatly appreciated and led to a much improved manuscript. We also thank Allan McNamara for a very fruitful discussion about convection. This research was supported by NASA grants NNX07AL30G and NNX08AL26G, and by the UCSC/Ames UARC program.

Appendix A. Implementation of melting and freezing

Here our implementation of melting and freezing of the ice shell is described in more detail.

Figures B.5a, B.5b and B.5c show the different stages of our melting calculation in more detail. We begin with an icy mantle, which is modeled in 3D via OEDIPUS, overlying a silicate core modeled through the 1D conduction code (Fig. B.5a). In this case, the codes share a common temperature point at the interface. Once the radially-averaged melt fraction at a particular level of OEDIPUS exceeds a threshold (here set to be 5 %), this level is removed from the OEDIPUS grid and added to the conduction code grid. Because the number of OEDIPUS grid-cells is kept constant, we recalculate the OEDIPUS grid size to account for the thinning of the solid ice shell, and interpolate the different fields (temperature, velocity and pressure) onto the updated grid. The level removed from OEDIPUS continues to melt in the 1D code according to equation 7. Heat transfer into and out of this level is calculated as follows. The bottom OEDIPUS point (R_j in Fig.B.5b) is set to the melting temperature, and the heat flux out of the level is set by the

temperature difference between R_j and R_{j+1}. The heat flux into the level is given by $F_c \left(\frac{R_c}{R_{j-1}}\right)^2$, as in the main text. Once melting at that level is complete, the heat flux from the ocean is assumed to impinge directly on the bottom OEDIPUS grid cell (Fig. B.5c), and the subsequent evolution of that cell is governed by equation 6.

When freezing occurs, a slightly different scheme must be employed. The location of the freezing front within the top conductive level is tracked. Since this point is at the melting point, the temperature at R_j ($T(equ.)$ in Fig.B.5b)) is then calculated by linear interpolation. Once the top conductive level is fully frozen, the OEDIPUS grid is expanded and the various fields are interpolated onto the updated grid. The process then repeats.

The procedures outlined above are discrete approximations of a continuum process. To check the freezing calculation, we compared the results with the classical (Cartesian) Stefan solution (e.g. Turcotte and Schubert, 2002) in the case with zero basal heat flux. Figure B.6a shows how the numerical results compare with the analytical case for different numbers of radial grid points N. The error decreases as N increases. For the melting case, we started with a solid shell and verified that, for a fixed basal heat flux, the equilibrium numerical shell thickness matched the expected analytical value (Fig. B.6b).

Appendix B. Benchmarks and Rayleigh number

Appendix B.1. OEDIPUS benchmark

To check that our code was working correctly, we compared it with the results of comparative studies of spherical, temperature-dependent viscosity

codes given by Stemmer et al. (2006) and Choblet et al. (2007). These solutions are given for two different Rayleigh numbers and perturbations. In all cases the dimensionless temperature is set to 0 at the surface and 1 at the inner boundary, the ratio of the inner over the outer radius is set to $f = R_1/R_0 = 0.55$ and the boundary conditions are free-slip. The Rayleigh number is defined at the viscosity given by a dimensionless temperature of 0.5. The first case uses a Rayleigh number of $Ra_{1/2}$=3500 and a cubic perturbation ($T(r,\theta,\phi) = T_i(r,\theta,\phi) + \epsilon Y_2^3(\theta,\phi) \times \sin(\pi(r - R_1))$) where T is the final temperature, T_i initial temperature, ϵ small perturbation, Y_l^m spherical harmonic of degree l and order m, r dimensionless radius and R_1 and R_0 dimensionless inner and outer radius, respectively while the second case uses a Rayleigh number of $Ra_{1/2}$=7000 and a tetrahedral perturbation ($T(r,\theta,\phi) = T_i(r,\theta,\phi) + \epsilon(Y_0^4(\theta,\phi) + 5/7 \quad Y_4^4(\theta,\phi)) \times \sin(\pi(r - R_1))$). Table B.5 summarizes these results and shows that our code's results are consistent with the previous ones.

Appendix B.2. Treatment of viscosity

The Rayleigh number in our model (equation 4) is defined at the base of the ice shell, at temperature T_b. It therefore depends on the viscosity at the base of the ice shell, η_b, where the temperature-dependence of the ice viscosity is given by an Arrhenius relationship (equation 8).

For numerical reasons, OEDIPUS is unable to deal with the extremely large viscosity contrasts between the base of the shell and the surface implied by the Arrhenius relationship. We define a reference temperature T_m = 273 K, a reference viscosity $\eta_m = \eta(T_m)$ and the ratio $avis_m$ between the surface viscosity η_{surf} and the reference viscosity: $\eta_{surf} = \eta_m \exp(avis_m)$. The

maximum value of $avis_m$ which OEDIPUS can run at is 14, equivalent to a viscosity ratio of $\sim 1.2 \times 10^6$.

We therefore calculate the viscosity within the shell using the full Arrhenius equation equation (8), but impose a maximum value of $\eta_b \exp(avis_m)$. Because this cutoff only applies to ice which is cold and highly viscous, the exact value of the cutoff is not expected to have any significant effect on the convective circulation.

Many numerical schemes (Solomatov, 1995, e.g.) replace the Arrhenius viscosity ($\eta_{\rm A}$) with the simpler Frank-Kamenetskii approximation ($\eta_{\rm FK}$). Near the reference temperature, these two descriptions result in similar viscosities, but at lower temperatures there is an increasing divergence. The temperature derivatives in the two cases are given by

$$\left.\frac{\partial \eta_{\rm FK}}{\partial T}\right|_{T=T_m} = \eta(T_m)\left(\frac{-avis_m}{T_m - T_{surf}}\right) \tag{B.1}$$

$$\left.\frac{\partial \eta_{\rm A}}{\partial T}\right|_{T=T_m} = \eta(T_m)\left(\frac{-E_a}{\mathcal{R}T_m^2}\right) \tag{B.2}$$

and setting the two equal results in an expression for $avis_m$:

$$avis_m = \left(\frac{E_a(T_m - T_{surf})}{\mathcal{R}T_m^2}\right) \tag{B.3}$$

Here T_{surf} is the surface temperature and E_a is the activation energy. For realistic ice parameters ($E_a = 50 - 60$ kJ mol^{-1}, $\mathcal{R} = 8.314$ J mol^{-1} K^{-1}, $T_m = 273$ K and $T_{surf} = 40$ K), we obtain $avis_m$=18.8-22.6, somewhat higher than the maximum value permitted by OEDIPUS.

Appendix B.3. Critical Rayleigh number

Following Solomatov (1995), the critical Rayleigh number in a strongly-temperature dependent fluid may be written as:

$$Ra_c = 20.9\ (xp)^4 \tag{B.4}$$

where x and $p = \gamma\ (T_b - T_{surf})$ are dimensionless parameters and here the Frank-Kamenetskii description of viscosity is being used: $\eta(T) = \eta_{surf}$ $\exp(-\gamma\ (T - T_{surf}))$. As long as $T_b = T_m$, equation (B.3) makes it clear that p=$avis_m$. Here Ra is being evaluated based on the viscosity at the base of the fluid (T_b).

Equation (B.4) was derived for a Cartesian geometry, in which case x=1. In a spherical shell, the different surface areas of the upper and lower boundaries would be expected to change the value of x. For instance, Barr and McKinnon (2007) studied the onset of convection on Enceladus and found that in this case $x \approx 2$, due to the temperature-dependent conductivity and spherical geometry. Here we focus on the latter effect.

To do so, we made two sets of simulations: the first with a viscosity law following the Frank-Kamenetskii approximation and the second with an Arrhenius law. In the latter case, as before we impose a maximum viscosity contrast of $\exp(p)$ across the fluid. Both sets have the same basal viscosity, free-slip boundary conditions and random initial perturbations. The initial temperature profile is set to the conductive solution. We then investigate three values of $f(= R_1/R_0)$: 0.9 to be as close as possible to a Cartesian case, 0.72 which is the value chosen for Pluto and 0.55 to have a low value. Moreover, in order to keep roughly the same dimension ratio for each cell

independent of the value of f, we used different resolutions (r, θ, ϕ) for each f: $16 \times 64 \times 64$ for $f = 0.9$, $32 \times 64 \times 64$ for $f = 0.72$ and $64 \times 64 \times 64$ for $f = 0.55$.

Fig B.7a plots Ra_c against p for different values of f with the Frank-Kamenetskii viscosity. The case with $f = 0.9$ closely resembles the expected Cartesian behaviour (equation B.4 with x=1, shown as the red line). As f decreases, the critical Rayleigh number increases, in agreement with Barr and McKinnon (2007). Fig B.7b plots results for the case with an Arrhenius viscosity. The critical Rayleigh number is shifted to systematically higher values compared with Fig B.7a. This is because the Arrhenius law results in vertically-averaged viscosities which are larger than with the F-K approximation. Nonetheless, we can obtain a reasonable fit to the data for f=0.72 by taking x=1.65 (green line). This value is somewhat smaller than the value of $x \approx 2$ obtained by Barr and McKinnon (2007), which is not surprising because for Enceladus $f \approx 0.65$.

In our numerical experiments we have $E_a = 60$ kJ mol^{-1} which implies p=22.6 (see above). Taking x=1.65 we find that $Ra_c \approx 4 \times 10^7$ from equation (B.4). Based on our definition of the Rayleigh number (equation 4), the basal viscosity η_b required for the onset of convection is approximately 1.7×10^{16} Pa s. That is broadly consistent with our numerical model results, in which convection is always encountered with a reference viscosity of 4.16×10^{15} Pa s, but not when the reference viscosity is 4.16×10^{17} Pa s.

References

Albrecht, R., Barbieri, C., Adorf, H., Corrain, G., Gemmo, A., Greenfield, P., Hainaut, O., Hook, R.N., Tholen, D.J., Blades, J.C., and Sparks, W.B. (1994). High-resolution imaging of the Pluto-Charon system with the Faint Object Camera of the Hubble Space Telescope. *Astrophys. J.*, 435, L75–L78.

Amelin, Y., Krot, A.N., Hutcheon, I.D., and Ulyanov, A.A. (2002). Lead isotopic ages of chondrules and calcium-aluminum-rich inclusions. *Science*, 297, 5587, 1678–1683.

Arakawa, M. and Maeno, N. (1994). Effective viscosity of partially melted ice in the ammonia-water system. *Geophys. Res. Lett.*, 21, 1515–1518.

Barr, A.C. and McKinnon, W.B. (2007a). Convection in Enceladus' ice shell: Conditions for initiation. *Geophys. Res. Lett.*, 34, L09202.

Barr, A. and McKinnon, W. (2007). Convection in ice I shells and mantles with self-consistent grain size. *J. Geophys. Res.*, 112, E11, E02012.

Bertoldi, F., Altenhoff, W., Weiss, A., Menten, K., and Thum, C. (2006). The trans-neptunian object UB313 is larger than Pluto. *Nature*, 439, 7076, 563–564.

Bills, B.G. and Nimmo, F. (2011). Rotational dynamics and internal structure of Titan. *Icarus*, 214, 1, 351–355.

Buie, M., Grundy, W., Young, E., Young, L., and Stern, S. (2006). Orbits

and photometry of Pluto's satellites: Charon, S/2005 P1, and S/2005 P2. *Astron. J.*, 132, 290–298.

Čadek, O. (2003). Viscoelastic relaxation of spherical Earth with a 3D viscosity structure. In *EGS-AGU-EUG Joint Assembly, Nice, France, 6-11 April 2003*, page 5279.

Canup, R.M. (2005). A giant impact origin of Pluto-Charon. *Science*, 307, 5709, 546–550.

Carslaw, H. and Jaeger, J. (1959). *Conduction of heat in solids*. Oxford University Press.

Castillo-Rogez, J., Matson, D., Sotin, C., Johnson, T., Lunine, J., and Thomas, P. (2007). Iapetus' geophysics: Rotation rate, shape, and equatorial ridge. *Icarus*, 190, 1, 179–202.

Castillo-Rogez, J.C. and Lunine, J.I. (2010). Evolution of Titan's rocky core constrained by Cassini observations. *Geophys. Res. Lett.*, 37, 20, L20205.

Choblet, G., Cadek, O., Couturier, F., and Dumoulin, C. (2007). OEDIPUS: A new tool to study the dynamics of planetary interiors. *Geophys. J. Int.*, 170, 1, 9–30.

Choblet, G. (2005). Modelling thermal convection with large viscosity gradients in one block of the 'cubed sphere'. *J. Comput. Phys.*, 205, 1, 269–291.

Ciesla, F. (2010). The distributions and ages of refractory objects in the solar nebula. *Icarus*, 208, 1, 455–467.

Cole, D.M. (1995). A model for the anelastic straining of saline ice subjected to cyclic loading. *Philo. Mag. A*, 72, 1, 231–248.

Collins, G.C. and Barr, A.C. (2008). Tectonics and interior structure of Pluto: Predictions from the orbital evolution of the Pluto-Charon system. In *AGU Fall Meeting Abstracts*, page 1425.

Collins, G.C. and Pappalardo, R.T. (2000). Predicted Stress Patterns on Pluto and Charon Due to Their Mutual Orbital Evolution. In *Lunar Planet. Sci. 31*, tome 31 of *Lunar and Planetary Institute Science Conference Abstracts*, page 1035.

Cook, J.C., Desch, S.J., Roush, T.L., Trujillo, C.A., and Geballe, T.R. (2007). Near-infrared spectroscopy of Charon: Possible evidence for cryovolcanism on Kuiper Belt Objects. *Astrophys. J.*, 663, 2, 1406–1419.

Cruikshank, D.P., Pilcher, C.B., and Morrison, D. (1976). Pluto: Evidence for methane frost. *Science*, 194, 4267, 835–837.

De La Chapelle, S., Milsch, H., Castelnau, O., and Duval, P. (1999). Compressive creep of ice containing a liquid intergranular phase: Rate-controlling processes in the dislocation creep regime. *Geophys. Res. Lett.*, 26, 251–254.

Desch, S.J., Cook, J.C., Doggett, T., and Porter, S.B. (2009). Thermal evolution of kuiper belt objects, with implications for cryovolcanism. *Icarus*, 202, 2, 694–714.

Dobrovolskis, A.R., Peale, S.J., and Harris, A.W. (1997). Dynamics of the

Pluto-Charon binary. In S. S.A. and T.D. J., editors, *Pluto and Charon*, pages 159–190. Arizona Press.

Durham, W.B., Kirby, S.H., and Stern, L.A. (1993). Flow of ices in the ammonia-water system. *J. Geophys. Res.*, 98, B10, 17667–17682.

Duval, P., Ashby, M.F., and Anderman, I. (1983). Rate-controlling processes in the creep of polycrystalline ice. *J. Phys. Chem.*, 87, 21, 4066–4074.

Efroimsky, M. and Williams, J. (2009). Tidal torques: A critical review of some techniques. *Celest. Mech. Dynam. Astron.*, 104, 3, 257–289.

Elliot, J.L., Dunham, E.W., Bosh, A.S., Slivan, S.M., Young, L.A., Wasserman, L.H., and Millis, R.L. (1989). Pluto's atmosphere. *Icarus*, 77, 1, 148–170.

Elliot, J.L., Person, M.J., Gulbis, A.A.S., Souza, S.P., Adams, E.R., Babcock, B.A., Gangestad, J.W., Jaskot, A.E., Kramer, E.A., Pasachoff, J.M., Pike, R.E., Zuluaga, C.A., Bosh, A.S., Dieters, S.W., Francis, P.J., Giles, A.B., Greenhill, J.G., Lade, B., Lucas, R., and Ramm, D.J. (2007). Changes in Pluto's atmosphere: 1988-2006. *Astron. J.*, 134, 1, 1–13.

Ellsworth, K. and Schubert, G. (1983). Saturn's icy satellites: Thermal and structural models. *Icarus*, 54, 3, 490–510.

Feistel, R. and Wagner, W. (2006). A new equation of state for H_2O ice Ih *J. Phys. Chem. Ref. Data*, 35, 2, 1021-1047.

Goldsby, D. and Kohlstedt, D. (2001). Superplastic deformation of ice: Experimental observations. *J. Geophys. Res.*, 106, 11017–11030.

Grasset, O. and Pargamin, J. (2005). The ammonia-water system at high pressures: Implications for the methane of Titan. *Planet. Space Sci.*, 53, 4, 371–384.

Hussmann, H., Choblet, G., Lainey, V., Matson, D., Sotin, C., Tobie, G., and Van Hoolst, T. (2010). Implications of rotation, orbital states, energy sources, and heat transport for internal processes in icy satellites. *Space Sci. Rev.*, pages 1–32.

Hussmann, H., Sohl, F., and Spohn, T. (2006). Subsurface oceans and deep interiors of medium-sized outer planet satellites and large trans-neptunian objects. *Icarus*, 185, 1, 258–273.

Hussmann, H., Spohn, T., and Wieczerkowski, K. (2002). Thermal equilibrium states of Europa's ice shell: Implications for internal ocean thickness and surface heat flow. *Icarus*, 156, 1, 143–151.

Jewitt, D.C. and Luu, J. (2004). Crystalline water ice on the Kuiper belt object (50000) Quaoar. *Nature*, 432, 7018, 731–733.

Kenyon, S.J. (2002). Planet formation in the outer solar system. *Publications of the Astronomical Society of the Pacific*, 114, 793, 265–283.

Kleine, T., Touboul, M., Bourdon, B., Nimmo, F., Mezger, K., Palme, H., Yin, Q.Z.and Jacobsen, S., and Halliday, A. (2009). Hf-W chronometry and the accretion and early evolution of asteroids and terrestrial planets. *Geochim. Cosmochim. Acta*.

Leliwa-Kopystynski, J., Maruyama, M., and Nakajima, T. (2002). The water-ammonia phase diagram up to 300 MPa: Application to icy satellites. *Icarus*, 159, 2, 518–528.

Lissauer, J.J. and Safronov, V.S. (1991). The random component of planetary rotation. *Icarus*, 93, 2, 288–297.

Lodders, K. (2003). Solar System abundances and condensation temperatures of the elements. *Astrophys. J.*, 591, 1220–1247.

Lunine, J.I. and Stevenson, D.J. (1987). Clathrate and ammonia hydrates at high pressure: Application to the origin of methane on Titan. *Icarus*, 70, 1, 61–77.

Malhotra, R. and Williams, J.G. (1997). Pluto's heliocentric orbit. In S.A. Stern and D.J. Tholen, editors, *Pluto and Charon*, pages 127–157. Arizona Press.

Manga, M. and Wang, C. (2007). Pressurized oceans and the eruption of liquid water on Europa and Enceladus. *Geophys. Res. Lett.*, 34, L07202.

McCord, T. and Sotin, C. (2005). Ceres: Evolution and current state. *J. Geophys. Res.*, 110, E05009.

McKinnon, W.B. (1989). On the origin of the Pluto-Charon binary. *Astrophys. J.*, 344, L41–L44.

McKinnon, W.B., Prialnik, D., Stern, S.A., and Coradini, A. (2008). Structure and Evolution of Kuiper Belt Objects and Dwarf Planets. In Barucci,

M.A. and Boehnhardt, H. and Cruikshank, D.P. and Morbidelli, A. , editor, *The Solar System Beyond Neptune*, pages 213–241. Arizona Press.

McKinnon, W., Simonelli, D., and Schubert, G. (1997). Composition, internal structure, and thermal evolution of Pluto and Charon. In S.A. Stern and D.J. Tholen, editors, *Pluto and Charon*, pages 295–343. Arizona Press.

McKinnon, W.B. (2006). On convection in ice I shells of outer Solar System bodies, with detailed application to Callisto. *Icarus*, 183, 2, 435–450.

Melosh, H.J. (1977). Global tectonics of a despun planet. *Icarus*, 31, 2, 221–243.

Mitri, G. and Showman, A.P. (2008). Thermal convection in ice-I shells of Titan and Enceladus. *Icarus*, 193, 387–396.

Moore, W.B. and Schubert, G. (2000). The tidal response of Europa. *Icarus*, 147, 1, 317–319.

Mottl, M.J., Glazer, B.T., Kaiser, R.I., and Meech, K.J. (2007). Water and astrobiology. *Chem. Erde*, 67, 4, 253–282.

Mousis, O., Gautier, D., and Bockelée-Morvan, D. (2002). An evolutionary turbulent model of Saturn's subnebula: Implications for the origin of the atmosphere of Titan. *Icarus*, 156, 1, 162–175.

Murray, C. and Dermott, S. (1999). *Solar System dynamics*. Cambridge University Press.

Nimmo, F. (2004). What is the young's modulus of ice? In P. Schenk, F. Nimmo, and L. Prockter, editors, *Workshop on Europa's Icy Shell: Past, Present, and Future*, page 7005.

Null, G. and Owen, Jr., W. (1996). Charon/Pluto mass ratio obtained with HST CCD observations in 1991 and 1993. *Astron. J.*, 111, 1368.

Ojakangas, G.W. and Stevenson, D.J. (1989). Polar wander of an ice shell on Europa. *Icarus*, 81, 2, 242–270.

Olkin, C.B., Wasserman, L.H., and Franz, O.G. (2003). The mass ratio of Charon to Pluto from Hubble Space Telescope astrometry with the fine guidance sensors. *Icarus*, 164, 254–259.

Owen, T.C., Roush, T.L., Cruikshank, D.P., Elliot, J.L., Young, L.A., Bergh, C.d., Schmitt, B., Geballe, T.R., Brown, R.H., and Bartholomew, M.J. (1993). Surface ices and the atmospheric composition of Pluto. *Science*, 261, 5122, 745–748.

Pasachoff, J.M., Souza, S.P., Babcock, B.A., Ticehurst, D.R., Elliot, J.L., Person, M.J., Clancy, K.B., Lewis C. Roberts, J., Hall, D.T., and Tholen, D.J. (2005). The structure of Pluto's atmosphere from the 2002 August 21 stellar occultation. *Astron. J.*, 129, 3, 1718–1723.

Peale, S.J. (1999). Origin and evolution of the natural satellites. *Annu. Rev. Astron. Astrophys.*, 37, 533–602.

Ransford, G.A., Finnerty, A.A., and Collerson, K.D. (1981). Europa's petrological thermal history. *Nature*, 289, 5793, 21–24.

Reeh, N., Lintz Christensen, E., Mayer, C., and Olesen, O. (2003). Tidal bending of glaciers: A linear viscoelastic approach. *Ann. Glaciol.*, 37, 83–89.

Roberts, J.H. and Nimmo, F. (2008). Tidal heating and the long-term stability of a subsurface ocean on Enceladus. *Icarus*, 194, 2, 675–689.

Robuchon, G., Choblet, G., Tobie, G., Cadek, O., Sotin, C., and Grasset, O. (2010). Coupling of thermal evolution and despinning of early Iapetus. *Icarus*, 207, 959–971.

Ronchi, C., Iacono, R., and Paolucci, P.S. (1996). The "cubed sphere": A new method for the solution of partial differential equations in spherical geometry. *J. Comput. Phys.*, 124, 1, 93–114.

Ross, R.G. and Kargel, J.S. (1998). Thermal conductivity of Solar System ices, with special reference to martian polar caps. In B. Schmitt, C. de Bergh, and M. Festou, editors, *Solar System Ices*, tome 227 of *Astrophysics and Space Science Library*, page 33. Kluwer Academic Publishers, Dordrecht/Boston/London.

Schubert, G., Hussmann, H., Lainey, V., Matson, D., McKinnon, W., Sohl, F., Sotin, C., Tobie, G., Turrini, D., and Van Hoolst, T. (2010). Evolution of icy satellites. *Space Sci. Rev.*, 153, 1, 447–484.

Schubert, G., Stevenson, D.J., and Ellsworth, K. (1981). Internal structures of the Galilean satellites. *Icarus*, 47, 1, 46–59.

Schulz, T., Münker, C., Mezger, K., and Palme, H. (2010). Hf-w chronometry of primitive achondrites. *Geochim. Cosmochim. Acta*, 74, 5, 1706–1718.

Shock, E.L. and McKinnon, W.B. (1993). Hydrothermal processing of cometary volatiles–applications to Triton. *Icarus*, 106, 2, 464–477.

Solomatov, V.S. (1995). Scaling of temperature- and stress-dependent viscosity convection. *Phys. Fluids*, 7, 266–274.

Sotin, C., Tobie, G., and J., W. (2009). Tides and tidal heating on Europa. In Pappalardo, McKinnon, and Khurana, editors, *Europa*, page 720. University of Arizona Press, Tucson, Arizona.

Spohn, T. and Schubert, G. (2003). Oceans in the icy Galilean satellites of Jupiter? *Icarus*, 161, 2, 456–467.

Stegman, D.R., Freeman, J., and May, D.A. (2009). Origin of ice diapirism, true polar wander, subsurface ocean, and tiger stripes of Enceladus driven by compositional convection. *Icarus*, 202, 2, 669–680.

Stemmer, K., Harder, H., and Hansen, U. (2006). A new method to simulate convection with strongly temperature- and pressure-dependent viscosity in a spherical shell: Applications to the earth's mantle. *Phys. Earth Planet. Inter.*, 157, 3-4, 223–249.

Stern, S.A. and Colwell, J.E. (1997). Accretion in the Edgeworth-Kuiper Belt: Forming 100-1000 km radius bodies at 30 AU and beyond. *Astron. J.*, 114, 2, 841–&.

Tanaka, M., Girard, G., Davis, R., Peuto, A., and Bignell, N. (2001). Recommended table for the density of water between 0 °C and 40 °C based on recent experimental reports. *Metrologia*, 38, 4, 301–309.

Tatibouet, J., Perez, J., and Vassoille, R. (1986). High-temperature internal friction and dislocations in ice Ih. *J. Phys. France*, 47, 1, 51–60.

Tholen, D. and Buie, M. (1990). Further analysis of Pluto-Charon mutual event observations - 1990. In *Bull. Am. Astron. Soc.*, tome 22 of *Bulletin of the American Astronomical Society*, pages 1129–1129.

Tobie, G., Cadek, O., and Sotin, C. (2008). Solid tidal friction above a liquid water reservoir as the origin of the south pole hotspot on Enceladus. *Icarus*, 196, 2, 642–652.

Tobie, G. and Cecconi, B. (2000). *Contraintes thermiques sur les satellites de glace de Saturne et Uranus*. Master thesis, University of Paris.

Tobie, G., Choblet, G., and Sotin, C. (2003). Tidally heated convection: Constraints on Europa's ice shell thickness. *J. Geophys. Res.*, 108(E11), 5124.

Tobie, G., Lunine, J.I., and Sotin, C. (2006). Episodic outgassing as the origin of atmospheric methane on Titan. *Nature*, 440, 7080, 61–64.

Turcotte, D. and Schubert, G. (2002). *Geodynamics - 2^{nd} edition*. Cambridge Editor.

Vance, S., Harnmeijer, J., Kimura, J., Hussmann, H., deMartin, B., and Brown, J.M. (2007). Hydrothermal systems in small ocean planets. *Astrobiology*, 7, 6, 987–1005.

Weaver, H.A., Stern, S.A., Mutchler, M.J., Steffl, A.J., Buie, M.W., Merline,

W.J., Spencer, J.R., Young, E.F., and Young, L.A. (2006). Discovery of two new satellites of Pluto. *Nature*, 439, 7079, 943–945.

Yoshida, M. and Kageyama, A. (2004). Application of the Yin-Yang grid to a thermal convection of a boussinesq fluid with infinite prandtl number in a three-dimensional spherical shell. *Geophys. Res. Lett.*, 31, 12609.

Zhong, S., Zuber, M., Moresi, L., and Gurnis, M. (2000). Role of temperature-dependent viscosity and surface plates in spherical shell models of mantle convection. *J. Geophys. Res.*, 105, 11063–11082.

Table B.1: Parameter values adopted. Thermal parameters for ice and silicates are taken from McCord and Sotin (2005) and Feistel, R. and Wagner, W. (2006). T is taken to T_m for thermal parameters of ice.

Table B.2: Relevant energy sources and sinks. The quantity ΔT_{eff} is the implied mean change in temperature of Pluto, assuming a bulk heat capacity of 1.7×10^{25} J K^{-1} (see Table B.1).

Table Captions

Table B.3: Radioactive species and decay data used in this study following compilation used by Robuchon et al. (2010). Concentrations are based on Carbonaceous chondrites following Lodders (2003).

Table B.4: Results of our simulations for six different reference viscosities and different initial temperatures. Negative and positive surface stresses mean respectively compressional and extensional stresses, evaluated at the present day.

Table B.5: Comparison of Nusselt numbers at the inner and outer boundaries (respectively Nu_{bot} and Nu_{top}) and rms velocities for 2 cases: Case 1: isoviscous case with $Ra_{1/2} = 3500$ and a cubic perturbation and Case 2: temperature-dependent viscosity ($\Delta\eta = 20$) with $Ra_{1/2} = 7000$ and a tetrahedral perturbation. The reference columns refers to the models used for comparison: Z00 (Zhong et al., 2000), Y04 (Yoshida and Kageyama, 2004), S06 (Stemmer et al., 2006), C07 (Choblet et al., 2007).

Figure B.1: a) Geometry of model set-up. The ice shell is modeled using the 3D OEDIPUS code and the silicate core with a 1D conduction model. b) Schematic of how melting is handled within OEDIPUS (see text).

Figure Captions

Figure B.2: a) Evolution of laterally-averaged temperature with time. The ice-silicate interface is at r=850 km; white-dashed line is 273 K contour. Ice shell convection initiates at 101 My and no ocean forms. Here the initial (uniform) temperature is 150 K and the ice reference viscosity is 10^{13} Pa s; other parameter values given in Table B.1. b) Evolution of surface heat flux (black line) and the conductive heat flux out of the silicate core evaluated at the surface (red line). The drop in core heat flux at 100 My is due to despinning heating the mantle. c) Pluto radius change as a function of time, and resulting elastic stresses (equation 17). Despinning occurs just after 100 My. Green line shows the boundary between compressional (-) and extensional (+) stresses. d) Evolution of spin period (from an initial period of 6 h) and resulting elastic equatorial stresses. Note that the horizontal axis is at a different scale to panels a-c. e) As for a), except that the reference viscosity is 4.16×10^{17} Pa s, the ice shell does not convect, an ocean develops at about 232 My and the present-day ocean thickness is 165 km. f) As for b). g) As for c). h) As for d).

Figure B.3: Evolution of different quantities of interest as a function of initial temperature and reference viscosity. Except for the lowest-viscosity case, the three panels at each reference viscosity represent initial temperatures of 150, 200 and 250 K (left to right). Black stars show when the ocean thickness equals 0. a) Evolution of RMS velocity in ice shell. Convection is assured with a reference viscosity of 4.16×10^{15} Pa s or lower, and never occurs at 4.16×10^{17} Pa s. b) Evolution of ocean thickness. Cases with low references viscosities never develop an ocean. c) Evolution of surface heat flux. Peak of heat flux is obtained when the ocean is the thickest. d) Evolution of surface stresses. Whether present-day stresses are compressional or extensional depend mainly on whether an ocean is present or not.

Figure B.4: a) Evolution of flattening for a case with [K] = 50 pp and a reference viscosity of 10^{14} Pa s. The red line is the model flattening, calculated using the methods described in Section 2.6; the green line is the flattening which would occur for a completely fluid body. In this case no ocean is present. Note the present-day fossil bulge. b) As for a), but for a case with the nominal potassium concentration and a reference viscosity of 10^{15} Pa s. In this case no ocean is present but the ice shell is convecting. Note the absence of a present-day fossil bulge. c) As for b), but in this case the reference viscosity is 4.16×10^{16} Pa s, the ice shell is conductive, an ocean is present, and there is no present-day fossil bulge.

Figure B.5: Sketches of different steps of melting calculation. a) When simulations begin the core heat flux is transferred into the icy mantle. b) When a melt layer is present the heat coming out of the core is transferred into the layer, and its evolution is tracked using the 1D conduction code. $T(equ.) = T(R_j)$ and is set to the melting point temperature when melting occurs, and is interpolated between the base of the freezing zone and the first grid point in OEDIPUS when freezing occurs (see text). c) When melting of that layer is complete, the heat flux F_c from the core is transferred to the base of the 3D convection code.

Figure B.6: a) Comparison of analytical Stefan model of ice freezing with numerical OEDIPUS results at different resolutions. b) Comparison of model equilibrium ice shell thickness at different resolutions for a specified CMB heat flux with the analytical solution. In both benchmarks thermal parameters are assumed constant: $k = 2.26$ W m^{-1} K^{-1}, $C_p = 2106$ J kg^{-1} K^{-1} and $L_a = 333$ J kg^{-1} (see Table B.1).

Figure B.7: Relation between curvature in spherical geometry and onset of convection for two different viscosity laws: a) Critical Rayleigh number as a function of p parameter (see equation B.4) for a temperature-dependent viscosity following the Frank-Kamenetskii approximation. b) Same as a) but for an Arrhenius law. Red curve on both figures show the analytical solution given by the equation B.4. Green curve on b) shows a fit of this equation with $x = 1.65$ for a Pluto case (f=0.72).

Figure1

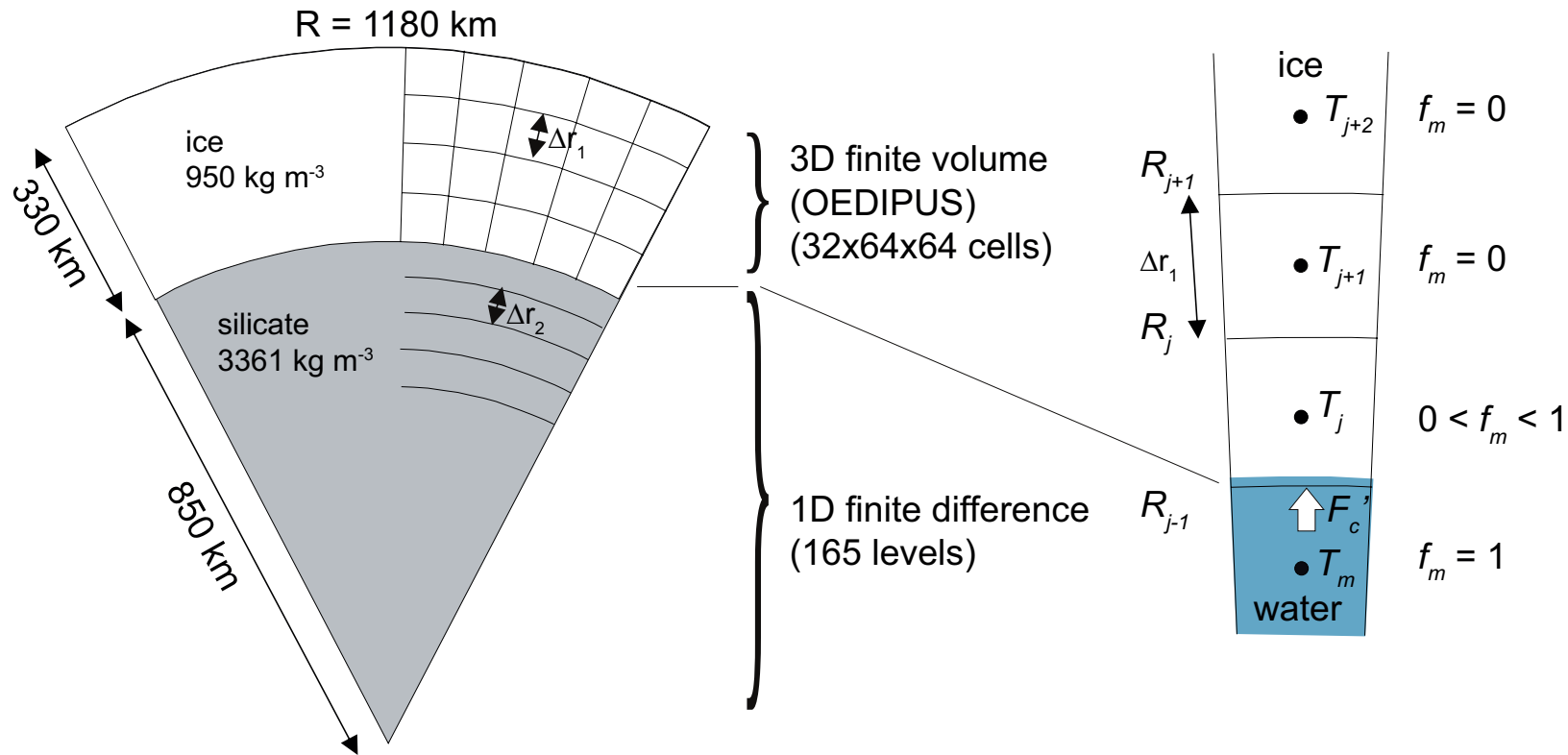
R = 1180 km
ice
950 kg m-3
silicate
3361 kg m-3
Δr1
Δr2
330 km
850 km
3D finite volume
(OEDIPUS)
(32x64x64 cells)
1D finite difference
(165 levels)
ice
Tj+2
fm = 0
Rj+1
Δr1
Rj
Tj+1
fm = 0
Tj
0 < fm < 1
Rj-1
Fc'
Tm
fm = 1
water

Figure2

Click here to download high resolution image

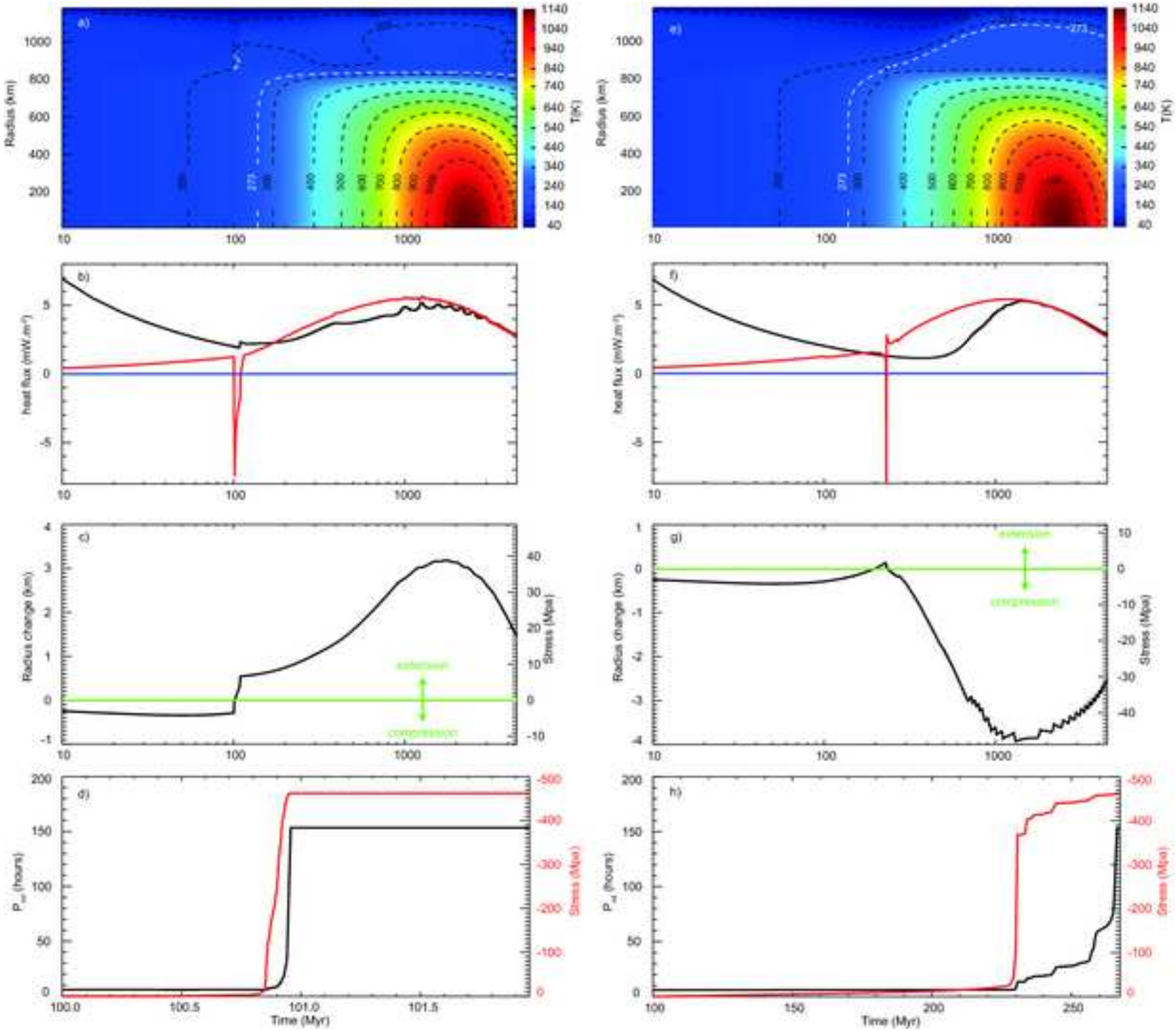

Figure3

Click here to download high resolution image

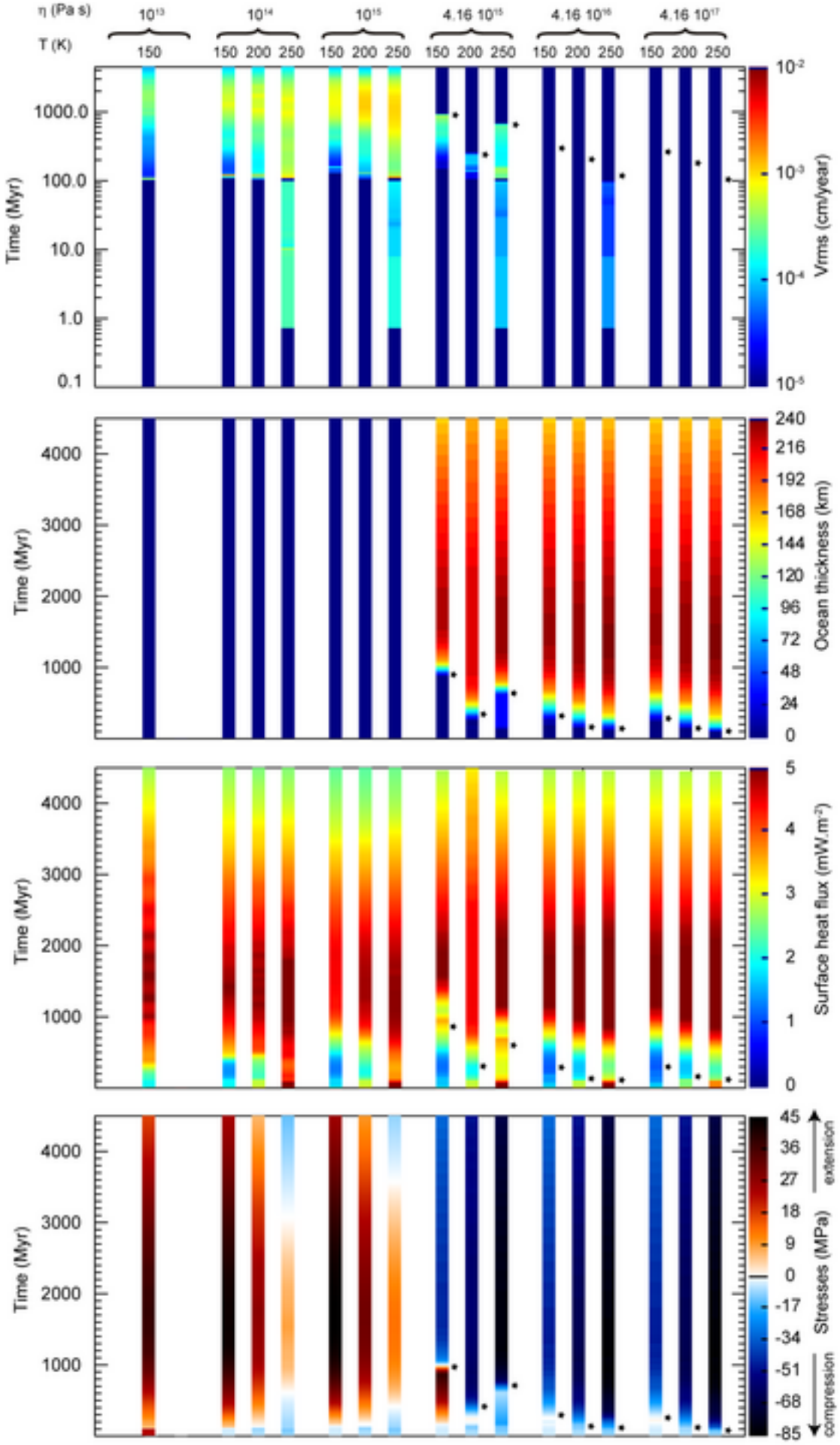

Figure4

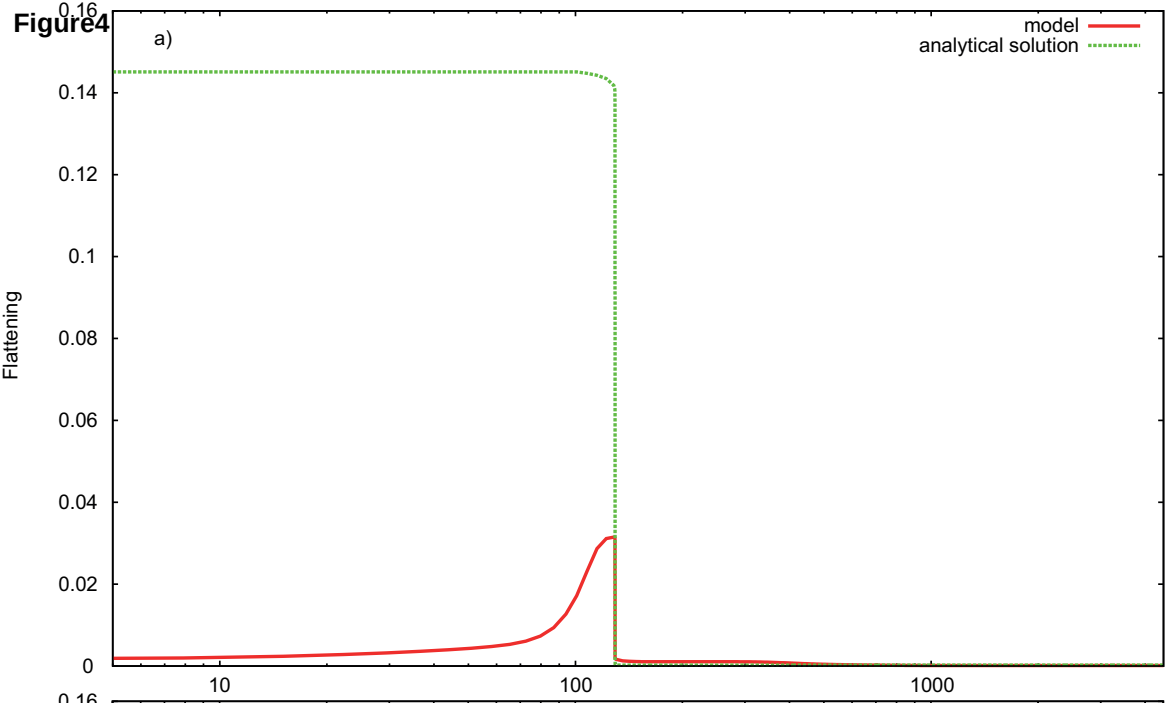
a)
model
analytical solution
Flattening
0.16
0.14
0.12
0.1
0.08
0.06
0.04
0.02
0
10
100
1000

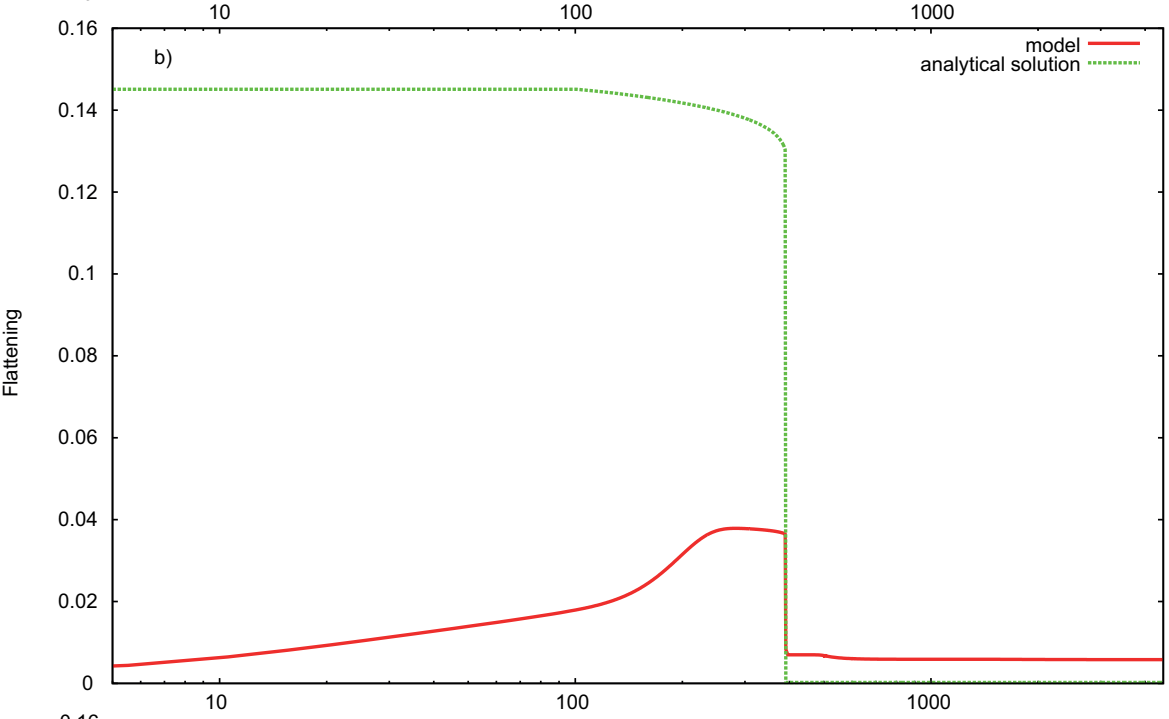
b)
model
analytical solution
Flattening
0.16
0.14
0.12
0.1
0.08
0.06
0.04
0.02
0
10
100
1000

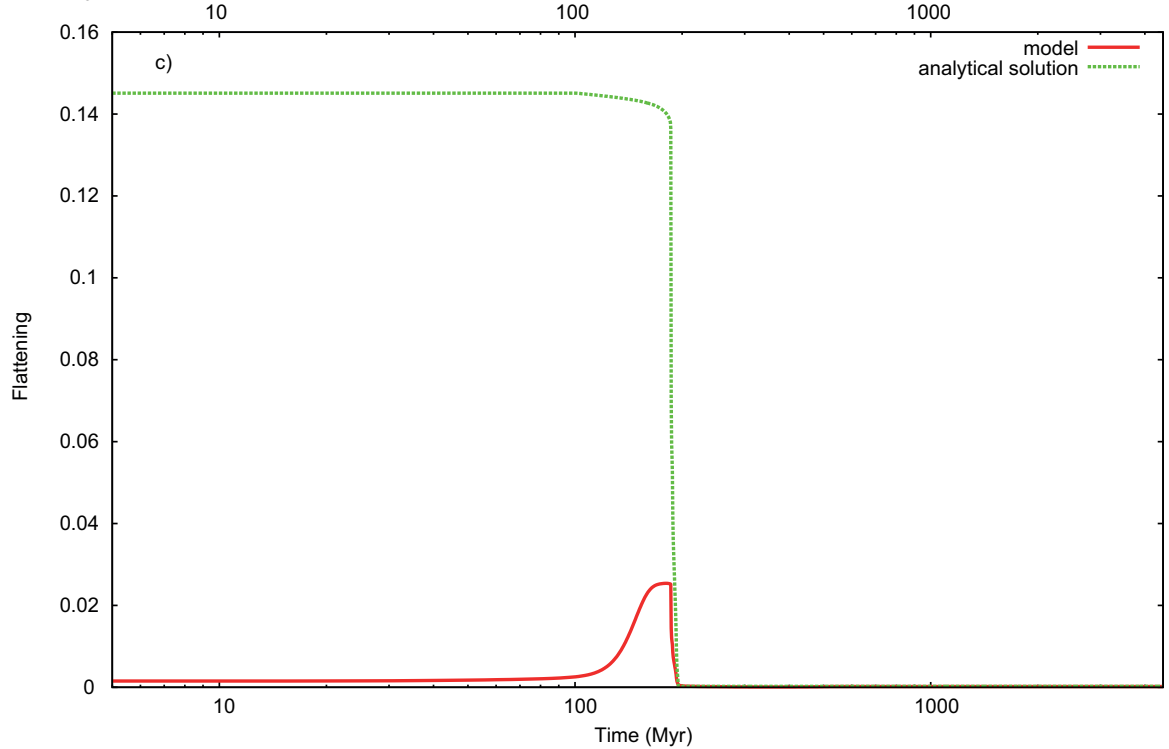
c)
model
analytical solution
Flattening
0.16
0.14
0.12
0.1
0.08
0.06
0.04
0.02
0
10
100
1000
Time (Myr)

Figure5

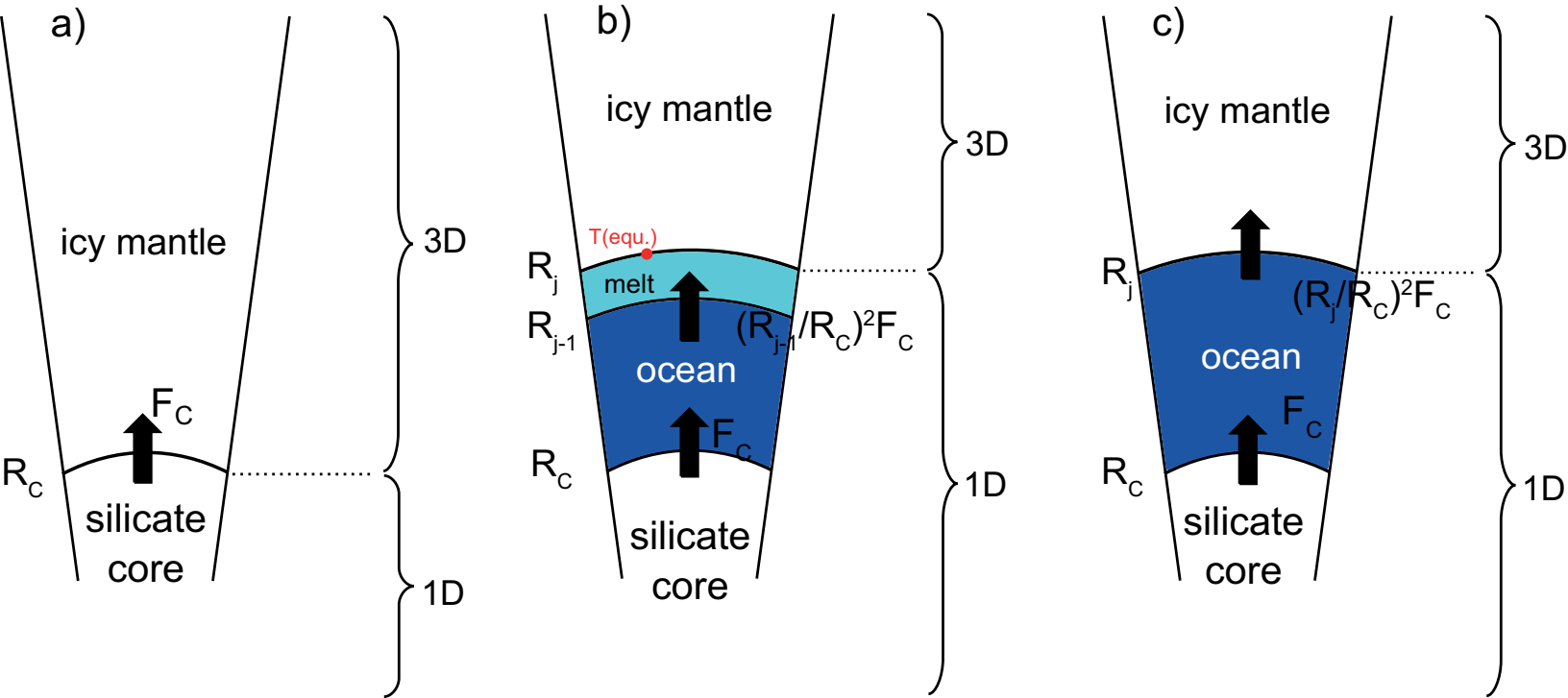
a)
icy mantle
3D
F_C
R_C
silicate
core
1D
b)
icy mantle
3D
T(equ.)
R_j
melt
R_{j-1}
$(R_{j-1}/R_C)^2F_C$
ocean
F_C
R_C
silicate
core
1D
c)
icy mantle
3D
R_j
$(R_j/R_C)^2F_C$
ocean
F_C
R_C
silicate
core
1D

Figure6

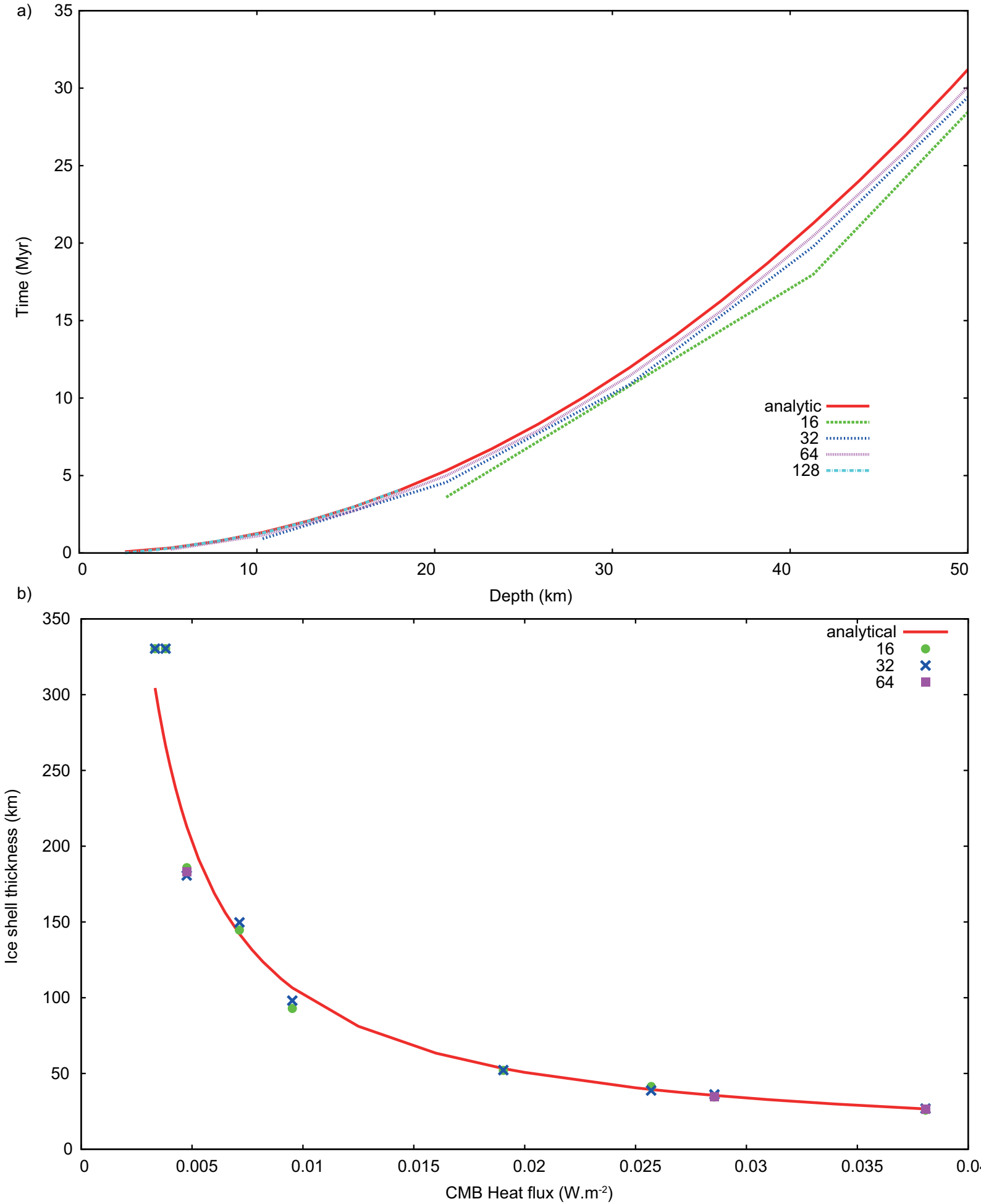
a)
Time (Myr)
Depth (km)
analytic
16
32
64
128
b)
Ice shell thickness (km)
CMB Heat flux (W.m-2)
analytical
16
32
64

Figure7

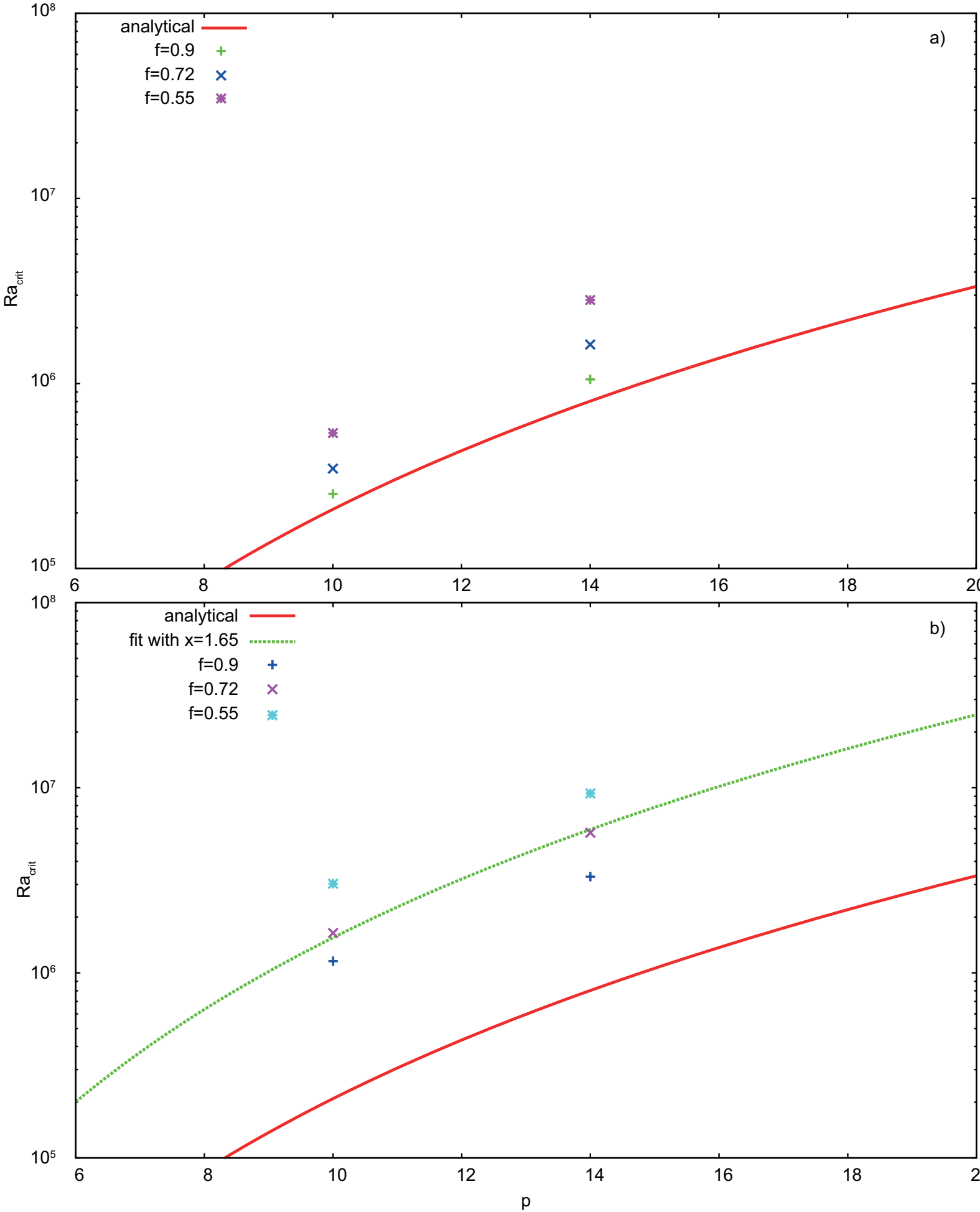
analytical
f=0.9
f=0.72
f=0.55
a)
10^8
10^7
10^6
10^5
Ra_{crit}
6
8
10
12
14
16
18
20
analytical
fit with x=1.65
f=0.9
f=0.72
f=0.55
b)
10^8
10^7
10^6
10^5
Ra_{crit}
6
8
10
12
14
16
18
20
p

Table1

Symbol	Associated quantity	Value	Unit
R	average radius	1180	km
R_c	average core radius	849.6	km
ρ_0	average density	1850	kg m^{-3}
T_m	reference temperature	273	K
T_{surf}	surface temperature	40	K
g_s	surface gravity	0.61	m s^{-2}
P_{rot}	spin period	6.38726	days
a	semi-major axis of the orbit	1.9705×10^4	km
M_c	Charon's mass	1.52×10^{21}	kg
E_a	activation energy	60	kJ mol^{-1}
η_m	reference viscosity	10^{13} to 4.16×10^{17}	Pa s
ρ_{ice}	ice density	950	kg m^{-3}
ρ_{wat}	water density	1000	kg m^{-3}
ρ_{sil}	silicate density	3361	kg m^{-3}
α_{ice}	thermal expansivity of ice	$1.56 \times 10^{-4}\ T/250$	K^{-1}
α_{sil}	thermal expansivity of silicate	2.4×10^{-5}	K^{-1}
κ	thermal diffusivity	$1.47 \times 10^{-6}\ (250/T)^2$	m^2 s^{-1}
k_{ice}	thermal conductivity of ice	$0.4685 + 488.12/T$	W m^{-1} K^{-1}
k_{sil}	thermal conductivity of silicate	4.2	W m^{-1} K^{-1}
L_a	ice latent heat	333	kJ kg^{-1}
μ_{ice}	shear modulus of ice	3.33×10^9	Pa

Table2

Energy	Value (J)	ΔT_{eff} (K)	Commentary
radioactive	1.30×10^{28}	780	released between 30 Myr and 4.5 Gyr after CAI formation (see Table 3)
accretion	5.70×10^{27}	340	$3GM^2/5R$
thermal	3.34×10^{27}	210	to warm up Pluto from 40 K to 250 K
despin	9.19×10^{26}	55	to slow down Pluto from 3h to the present-day period
differentiation	8.37×10^{26}	49	to differentiate into a two layer structure (Hussmann et al., 2010)
latent heat	7.20×10^{26}	43	to melt 200 km of ice close to the CMB

Table3

Element	Half-life τ_0 (Myr)	Concentration C (ppb)	H_0 (W/Kg of element)
^{238}U	4468	19.9	94.65×10^{-6}
^{235}U	703.81	5.4	568.7×10^{-6}
^{232}Th	14030	38.7	26.38×10^{-6}
^{40}K	1277	738	29.17×10^{-6}

Table4

Reference viscosity (Pa s)	10^{13}			10^{14}			10^{15}		
Initial temperature (K)	150			150	200	250	150	200	250
onset of convection (Myr)	101			106	100	101	130	101	100
end of convection (Myr)	/			/	/	/	/	/	/
onset of ocean (Myr)	/			/	/	/	/	/	/
current ocean thickness (km)	0			0	0	0	0	0	0
current surface heat flux (mW m^{-2})	2.71			2.65	2.56	2.59	2.42	2.38	2.48
surface stresses due to volume change (MPa)	18			25	7	-13	26	10	-9
Reference viscosity (Pa s)	4.16×10^{15}			4.16×10^{16}			4.16×10^{17}		
Initial temperature (K)	150	200	250	150	200	250	150	200	250
onset of convection (Myr)	177	128	27	no	no	40	no	no	no
end of convection (Myr)	930	800	708	no	no	105	no	no	no
onset of ocean (Myr)	875	255	125	186	145	115	232	140	95
current ocean thickness (km)	165	165	165	165	165	165	165	165	165
current surface heat flux (mW m^{-2})	2.8	2.8	2.8	2.8	2.8	2.8	2.8	2.8	2.8
surface stresses due to volume change (MPa)	-31	-50	-68	-30	-49	-68	-30	-49	-68

Table5

Reference	Resolution	Case 1			Case 2		
		Nu_{top}	Nu_{bot}	V_{rms}	Nu_{top}	Nu_{bot}	V_{rms}
Y04	102x102x104	2.8830	-	18.4801	3.133	-	26.1064
S06	6x48x48x48	-	-	-	3.1447	3.1450	25.73
C07	6x32x32x32	2.8640	2.8948	19.546	-	-	-
our benchmarks	6x32x32x32	2.923	2.922	19.37	3.1110	3.1113	24.66